Coupled interactions between volatile activity and Fe oxidation state during arc crustal processes

Humphreys, M.C.S.[1,2], Brooker, R.A.[3], Fraser, D.G.[2], Burgisser, A.[4], Mangan, M.T.[5] & McCammon, C.[6]

[1] Department of Earth Sciences, Durham University, Science Labs, Durham, DH1 3LE
Email: madeleine.humphreys@durham.ac.uk; Tel: +44(0)191 334 2300; Fax: +44 (0)191 334 2301

[2] Department of Earth Sciences, University of Oxford, South Parks Road, Oxford, OX1 3AN, UK

[3] School of Earth Sciences, University of Bristol, Wills Memorial Building, Queen's Road, Bristol, BS8 1RJ, UK

[4] Institut des Sciences de la Terre d'Orléans, CNRS, Université d'Orléans, 1A Rue de la Férollerie, 45071 Orléans CEDEX 2, France

[5] US Geological Survey, 345 Middlefield Road, Menlo Park, CA 94025-3561, USA

[6] Bayerisches Geoinstitut, Universität Bayreuth, D-95440 Bayreuth, Germany

ABSTRACT

Arc magmas erupted at the earth's surface are commonly more oxidised than those produced at mid-ocean ridges. Possible explanations for this high oxidation state are that the transfer of fluids during the subduction process results in direct oxidation of the sub-arc mantle wedge; or that oxidation is caused by the effect of later crustal processes, including protracted fractionation and degassing of volatile-rich magmas. This study sets out to investigate the effect of disequilibrium crustal processes that may involve coupled changes in H_2O content and Fe oxidation state, by examining the degassing and hydration of sulphur-free rhyolites. We show that experimentally hydrated melts record strong increases in $Fe^{3+}/\Sigma Fe$ with increasing H_2O concentration as a result of changes in water activity. This is relevant for the passage of H_2O-undersaturated melts from the deep crust towards shallow crustal storage regions, and raises the possibility that vertical variations in fO_2 might develop within arc crust.

Conversely, degassing experiments produce an increase in $Fe^{3+}/\Sigma Fe$ with decreasing H_2O concentration. In this case the oxidation is explained by loss of H_2 as well as H_2O into bubbles during decompression, consistent with thermodynamic modelling, and is relevant for magmas undergoing shallow degassing *en route* to the surface. We discuss these results in the context of the possible controls on fO_2 during the generation, storage and ascent of magmas in natural arc settings, in particular considering the timescales of equilibration relative to observation as this affects the quality of the petrologic record of magmatic fO_2.

INTRODUCTION

A fundamental question in earth sciences concerns the distribution of oxygen within the solid Earth, its cycling through subduction zones and, through volcanic degassing, its effects on the atmosphere. In particular, the controls on the oxidation state of melts as they pass through the mantle and crust are challenging to constrain. It is clear that transfer of hydrous fluids from the subducting slab into the mantle is crucial for generating some of the typical geochemical signatures of subduction zone magmas, such as enrichment in large ion lithophile elements (LILE) and volatiles. Comparison of $Fe^{3+}/\Sigma Fe$ in lavas arriving at the Earth's surface shows that arc lavas also tend to be more oxidised than those produced at mid-ocean ridges or in other settings (e.g. Carmichael 1991; Ballhaus 1993; Lee et al. 2010; Evans et al. 2012). Mantle xenoliths entrained by arc magmas also appear to be more oxidised than those in other tectonic environments (e.g. Wood et al. 1990; Brandon & Draper 1996; Parkinson & Arculus 1999; Frost & McCammon 2008).

It is commonly suggested that increased fO_2 in arc systems compared with other tectonic environments is a primary feature related to mass transfer from the subducting slab to the mantle wedge (e.g. Brandon & Draper 1996; Parkinson & Arculus 1999; Kelley & Cottrell 2009), either directly through addition of volatiles, or indirectly if hydrous fluids carry dissolved Fe^{3+} or sulphate (Kelley &

65 Cottrell 2009). However, subduction zone magmatism is also characterised by
66 complex crustal processes that could be expected to exert significant controls on
67 oxidation state. These processes include magma fractionation, decompression,
68 degassing and eruption. Arc magmas tend to be volatile rich and may be more
69 prone to stalling and storage in the crust during ascent; this may increase the
70 importance of fractionation and degassing in particular. Arc magmas also tend to
71 crystallise magnetite early during differentiation, and studies based on the
72 partitioning of redox-sensitive incompatible elements suggest that magmatic
73 differentiation could be one reason for the higher $Fe^{3+}/\Sigma Fe$ of arc lavas (e.g.
74 Mallman & O'Neill 2009; Lee et al. 2010). Other studies suggest that the influence
75 of volatiles on fO_2 could be significant, particularly during crustal processes such
76 as the degassing of C-O-H-S volatile species during shallow magmatic ascent (e.g.
77 Sato 1978; Mathez 1984; Candela 1986; Burgisser & Scaillet 2007; Burgisser et
78 al. 2008; Fiege et al. 2014).

79 Understanding the relationship between volatiles and the oxidation state
80 of magmas involves untangling two distinct problems. The first problem is the
81 fundamental effect of dissolved volatiles, as chemical constituents of the melt, in
82 determining Fe oxidation state. This is at the heart of whether H_2O can itself be
83 an important oxidising agent, or whether the observed link between H_2O and
84 $Fe^{3+}/\Sigma Fe$ is possible only by association with oxidised components in slab fluids
85 (e.g. Lecuyer & Ricard 1996; Parkinson & Arculus 1999). The second problem is
86 to understand the ways in which crustal processes may affect both melt volatile
87 concentrations and melt oxidation state. These effects include (i) variations in
88 *equilibrium* volatile speciation and Fe redox state with pressure and
89 temperature, and (ii) factors related to processes such as magmatic degassing;
90 these factors could be truly *disequilibrium* (i.e., kinetically inhibited over the
91 time- and length-scale of interest) or *open system* (for example, involving
92 segregation of melt and vapour).

93 In Part I of this study we present a brief review of literature evidence
94 relating to the first problem, that of chemical mechanisms linking volatile
95 dissolution with melt oxidation state, to consider whether volatiles can
96 fundamentally affect oxidation state *via* melt chemistry. In Part II, we tackle the

second problem, presenting new data to explore the effect of disequilibrium or open system changes in H_2O content on the oxidation state of sulphur-free rhyolite melts and glasses, using a new series of coupled H_2O and $Fe^{3+}/\Sigma Fe$ measurements from existing hydration and decompression experiments. We discuss the implications of our results for processes operating in natural magmas, highlighting the need to consider kinetics in these arc systems where there is ample evidence of disequilibrium at a variety of temporal and spatial scales.

PART I: A REVIEW OF THE EVIDENCE LINKING VOLATILES, MELT CHEMISTRY AND OXIDATION STATE

The effects of variations in anhydrous melt composition on ferric-ferrous ratios at constant fO_2 are well known (e.g. Paul & Douglas 1965; Sack et al. 1980; Kress & Carmichael 1991; Toplis 2005), but there has been considerable debate over the effect of H_2O, as a chemical component of the melt, on $Fe^{3+}/\Sigma Fe$. In particular, it has been suggested that the same process that causes oxidation when alkalis are added into silicate melts at constant fO_2 (e.g. Paul & Douglas 1965) should also operate during dissolution of volatile species (Fraser 2005; Moretti 2005; Toplis 2005), by altering the relative activity coefficients of Fe^{2+} and Fe^{3+} species within the melt.

This relies on the quasi-chemical theory defined by the Lux-Flood 'basicity' of different oxide components. This considers equilibrium between bridging oxygens (O^0), non-bridging oxygens (O^-) and 'free oxide' anions that are not bonded to the tetrahedral silicate polymer network (O^{2-}, Toop & Samis 1962). In this model, the melt is a molten ionic solution dominated by oxide ions (Flood & Förland 1947; Fraser 1975; Duffy 1993; Ottonello et al 2001; Moretti 2005; Fraser 2005). Interaction between oxygen in different structural positions:

$$O^0 + O^{2-} = 2O^- \qquad [1]$$

defines the basicity of the solution. Basic oxides such as alkalis (Na_2O or K_2O) dissociate to supply O^{2-} to the system and hence drive depolymerisation (breaking of oxo-bridges; equilibrium [1] moves to the RHS) while acidic oxides

(such as SiO_2) react with O^{2-} to form polymer chains. Amphoteric oxides, including Fe_2O_3, Al_2O_3, H_2O and CO_2 (Fraser 1977), can act as an acid or a base depending on the composition of the silicate solution (Kushiro 1975). Fe oxide components in the silicate melt therefore have the following possible reactions (neglecting acidic behaviour of FeO, Fraser 1975; 2005):

$$FeO = Fe^{2+} + O^{2-} \quad \text{[basic, 2a]}$$

$$Fe_2O_3 = 2Fe^{3+} + 3O^{2-} \quad \text{[basic, 2b]}$$

$$Fe_2O_3 + O^{2-} = 2FeO_2^- \quad \text{[acidic, 2c]}$$

where FeO_2^- is part of the structural network, analogous to AlO_4^-.

Some evidence suggests that the dissolution of H_2O in polymerised silicate melts occurs by a depolymerisation reaction with the tetrahedral network by breaking of T-O-T bridges to form shorter polymer chains terminated by –OH (e.g. Stolper 1982; Xue & Kanzaki 2006; Malfait et al. 2014; though also see Kohn 2000), as well as by incorporation of unreacted molecular H_2O (e.g. Burnham 1975; Stolper 1982). This suggests that in these cases, dissolved H_2O should also show basic behaviour, similar to K_2O or Na_2O (in addition to the incorporation of unreacted, molecular water):

$$H_2O + O^0 = 2OH \quad \text{[basic, 3b]}$$

In strongly basic melts, it was predicted that H_2O could also behave as an acidic oxide (Yokokawa 1986; Fraser 1977; Fraser 2005; Moretti 2005):

$$H_2O + O^{2-} = 2OH^- \quad \text{[acidic, 3a]}$$

where OH^- is "free hydroxyl" that is not bound to the silicate network but complexed with metal cations. This is supported by ^1H NMR experiments (Xue & Kanzaki 2004) and may contribute to variations in solubility with silicate melt composition (Yokokawa 1986). Similar reactions are suggested for dissolution of CO_2, and this is supported by variations in carbon speciation with melt basicity (Brooker et al. 1999) as well as NMR and Raman spectroscopy studies (Mysen et al. 2011).

Linking H_2O solubility, melt basicity and oxidation state

In silicate melts, the ratios of multi-valent ions such as Eu^{3+}/Eu^{2+} increase with increasing melt basicity (aO^{2-}) at constant fO_2 (Morris & Haskin 1974; Tilquin et al. 1997). This is consistent with thermodynamic constraints if amphoteric behaviour of Fe oxide components is considered (reactions 2a-c, Fraser 1975), and explains the observed increase of Fe^{3+}/Fe^{2+} with increasing alkali (or basic oxide) content of the melt (e.g. Paul & Douglas 1965; Sack et al. 1980; Kress & Carmichael 1991; Toplis 2005). Increasing the availability of free oxide (O^{2-}) leads to an overall net decrease of aFe_2O_3(m) from reactions 2b and 2c while simultaneously increasing $aFeO$ (m) from reaction 2a. This produces an overall increase in $Fe^{3+}/\Sigma Fe$ at constant fO_2, and should also polymerise the melt structure, because of the contribution of FeO_2^- to the melt framework (Fraser 1977; Ottonello et al. 2001; Fraser 2005; Moretti 2005).

For volatiles, the same approach predicts that (basic) reaction of H_2O with the silicate melt to form dissolved -OH [3b] should result in a net increase in aO^{2-} (and hence increasing $Fe^{3+}/\Sigma Fe$) whereas (acidic) formation of free hydroxyl in very basic melts [3a] results in a net decrease in aO^{2-} (and hence decreased $Fe^{3+}/\Sigma Fe$). Similarly, dissolution of carbon dioxide in basic melts should result in net decrease in aO^{2-}, and thus decreasing $Fe^{3+}/\Sigma Fe$. This provides a testable link between volatile solution mechanisms and melt oxidation state, which we review below.

Previous work on Fe^{3+}/Fe^{2+} in hydrous melts

Several previous studies have attempted to discern differences in redox state between equivalent hydrous and anhydrous melt compositions, with somewhat equivocal results. Moore et al. (1995) found no effect of H_2O on the Fe oxidation state of hydrous peralkaline rhyolites, supporting an earlier study (Sisson & Grove 1993) that compared $Fe^{3+}/\Sigma Fe$ in hydrous basalts with the anhydrous predictions of the Kress & Carmichael (1991) model. Botcharnikov et al. (2005) concluded that $Fe^{3+}/\Sigma Fe$ in hydrous ferrobasalt was mainly controlled experimentally by aH_2O (and hence fO_2) and was within the range predicted by existing anhydrous models.

In contrast, Gaillard et al. (2001) showed that addition of up to 6 wt% H_2O has an oxidising effect on metaluminous rhyolite relative to Kress & Carmichael (1991), but only at lower fO_2 conditions (<NNO+1). Gaillard et al. (2003a) also observed higher $Fe^{3+}/\Sigma Fe$ in hydrous *vs* anhydrous rhyolite and ascribed this to a decrease in the ratio of activity coefficients ($\gamma_{Fe2O3}^{L}/\gamma_{FeO}^{L}$) in hydrous melts, or decreasing a_{Fe2O3}^{L} for a given XFe_2O_3 and increasing a_{FeO}^{L} for a given XFeOL. This is essentially the same effect as predicted by acid-base theory (as described above). Schuessler et al. (2008) found that $Fe^{3+}/\Sigma Fe$ increased with H_2O content at constant fO_2 in hydrous phonotephrites, which they attributed to the effects of melt basicity as described by Ottonello et al. (2001) and Moretti (2005). These principles are also supported by observations of differences in olivine-melt K_D^{Fe-Mg} in hydrous and anhydrous melts (Toplis 2005).

Thus, while the results are still unclear, it does seem possible that H_2O has a resolvable effect on melt $Fe^{3+}/\Sigma Fe$ through behaviour that is similar to the basic metal oxides (e.g. K_2O). Such an effect is probably minor, but would be most important in relatively polymerised melts and at high pressures where variations in oxidation state could affect the compositions of minerals that could fractionate Fe^{2+} from Fe^{3+}. This would appear to justify further work in the context of hydrous subduction zone melts. Finally, the basicity approach highlights that oxidation state should be considered alongside an understanding of melt chemical species and melt structure.

PART II: EFFECT OF VARYING VOLATILE CONTENTS ON OXIDATION STATE

The second part of this paper specifically addresses how variations in melt volatile concentrations during crustal processes may affect melt $Fe^{3+}/\Sigma Fe$. We seek to explore two key processes in particular: (i) dehydration or degassing of volatiles during decompression, and (ii) hydration, due to H_2O-undersaturated magma ascent from high pressures. We present new XANES $Fe^{3+}/\Sigma Fe$ analysis for two sets of existing experimental samples to investigate these processes: a set of decompression experiments from the study of Mangan & Sisson (2000),

and a set of partial hydration experiments from Humphreys et al. (2008). A brief description of the experimental procedures is included below.

Decompression and H_2O degassing experiments

Samples of the experimentally degassed Panum Crater Dome obsidian were taken from the study of Mangan & Sisson (2000; table 1). The starting materials for these experiments were slabs of obsidian, loaded into Pt capsules together with excess H_2O. The samples were superheated at 1000 °C for several hours in Hf-Zr-Mo cold-seal pressure vessels at 200 MPa, pressurised using Ar gas, then equilibrated at 900 °C for three days, and finally decompressed isothermally at 0.025 MPa/s to variable final pressure (P_f) and immediately quenched. Decompression runs lasted 17 to 117 minutes. There was no attempt to buffer fO_2 but rapid H_2 diffusion through the Pt capsule would have equilibrated the samples at a high fO_2 during the initial 3-day heating. Any observed covariance between H_2O loss and $Fe^{3+}/\Sigma Fe$ over short lengthscales in the samples must therefore be related to the short decompression phase of the experiment. The resulting glasses are variably vesicular, with bubbles nucleating throughout the capsule in some runs, but only at the margins of the capsule in others (table 1; Mangan & Sisson 2000). Most of the samples analysed by XANES contained primarily marginal bubbles. H_2O contents and vesicularity data clearly demonstrate that bubble nucleation was delayed and did not occur at equilibrium (Mangan & Sisson 2000), yielding a suite of glasses with heterogeneous H_2O contents over short lengthscales. The anhydrous composition of the glass is constant within analytical uncertainty (table 2), indicating that no other compositional changes to the melt occurred during degassing.

Partial hydration experiments

To compare the mechanisms of hydration and H_2O degassing, we analysed partially hydrated Lipari obsidian cores as reported in Humphreys et al. (2008). The starting materials for these experiments were cylinders of homogeneous

Lipari obsidian, which were loaded into gold capsules with excess H_2O, along with a small amount of finely ground obsidian powder to prevent dissolution of the glass during the experiment. The capsules were then held at super-liquidus conditions, 150-200 MPa and 855-905 °C in cold-seal pressure vessel apparatus pressurised by water. Run times were short (20-80 minutes) and achieved partial hydration of the glass cylinders (table 1; Humphreys et al. 2008). No double capsule oxygen buffer control was used during the experiments but the short run times, low temperatures and use of Au capsules effectively ensure impermeability to H_2 during the experiments (Chou 1986). The anhydrous composition of the glass is constant within analytical uncertainty (table 2), indicating that hydration is not associated with any other compositional changes to the melt.

ANALYTICAL METHODS

X-ray Absorption Near Edge Structure (XANES)

$Fe^{3+}/\Sigma Fe$ of experimental glasses were measured using Fe K-edge micro X-ray Absorption Near Edge Structure (μXANES) spectroscopy on the I18 (Microfocus Spectroscopy) beamline at the Diamond Light Source, UK. Spectra were recorded in fluorescence mode and the beam size at the sample was approximately 3 x 5 μm. The beamline uses a Si(111) crystal monochromator which gives an energy resolution ($\Delta E/E$) of 1.4×10^{-4} (approximately 1 eV at the Fe K-edge); the energy stability of the beamline is ±0.05 eV per day. Fluorescence X-rays were normalised to the incident beam flux and collected using a 9-element solid state detector. The energy was calibrated by defining the first peak of the first derivative of Fe foil to be at 7112 eV (or 7111.1 eV for comparison with older published literature data, e.g. Wilke et al. 2001). Spectra were recorded from 7028 eV to 7400 eV using a 0.086 eV step over the pre-edge region (7098-7123 eV), 0.259 eV step across the edge (7123-7158 eV) and ~5 eV step to define both the baseline (7028-7098 eV) and the post-edge region. Initial spectra were collected up to 7340 eV but this was extended out to 7400 eV in later runs to aid

the normalisation procedure (see below). Counting times were 2000 msec on all points. The locations of all points analysed were recorded carefully with reference to reflected light images of the samples to enable accurate relocation for later SIMS analyses of the same points.

$Fe^{3+}/\Sigma Fe$ measurements were quantified by referencing the centroid energy of the pre-edge feature to a linear calibration (Figure 1a) constructed using a suite of anhydrous rhyolite glass standards that were synthesised at 1 atm and a range of fO_2 (FMQ+0.8 to +6) and $Fe^{3+}/\Sigma Fe$ from 0.238 to 0.806 (Cottrell et al. 2009; table 3). The raw spectra were normalised by fitting a straight line to both the low-energy baseline and the post-edge region, using the *Athena* software package (Ravel & Newville 2005). The pre-edge feature in Fe spectra typically shows two overlapping peaks whose centroid energy is quantitatively proportional to redox state (e.g. Wilke et al. 2001; Berry et al. 2003; Cottrell et al. 2009). The pre-edge regions of the normalised spectra were fitted between 7106 and ~7118 eV, using a cubic baseline plus a Gaussian to define the rising background towards the main K-edge, and two additional Gaussian peaks to define the pre-edge region (following Berry et al. 2003; Cottrell et al. 2009).

SIMS and EPMA

Glasses were analysed for $^{1}H^{+}$, $^{7}Li^{+}$, $^{12}C^{+}$, $^{25}Mg^{+}/2$, $^{16}O^{1}H^{+}$, $^{19}F^{+}$, $^{23}Na^{+}$, $^{26}Mg^{+}$, $^{30}Si^{+}$, $^{35}Cl^{+}$ and $^{29}K^{+}$ using the CAMECA ims 4f secondary ion mass spectrometer at the University of Edinburgh. NIST SRM610 was used as the primary calibration standard; $^{30}Si^{+}$ was the internal standard. Mass 0.7 was used to monitor the background count rate of the electron multiplier detector. A 10 kV, 2 nA, O^{-} primary beam was accelerated onto the sample with a net impact energy of 14.5 kV. Secondary ions were extracted at +4.5 eV using a 75 V offset. A pre-sputter period of approximately 2 minutes, with a nominal 15 μm rastered beam, was used to clean the sample surface, during which time the mass spectrometer was calibrated for the secondary ions. For quantitative analysis, the focused beam was reduced to ~10 μm using a field aperture. H_2O contents of the glass were derived using a daily working curve (figure 1b) of measured $^{1}H^{+}/^{30}Si^{+}$ *vs.* H_2O in

well-calibrated hydrous glass standards, following the methods of Blundy & Cashman (2005). Typical errors in determining H_2O are ~8-12% relative. Where possible, the same points analysed by XANES were targeted for SIMS measurements. Major element glass compositions were analysed using a 5-spectrometer Cameca SX-100 electron microprobe at the University of Cambridge, with a defocused (15 μm), 15 kV, 4 nA electron beam for major elements and a 10 nA beam for minor elements. Other analytical conditions were equivalent to those of Humphreys et al. (2006a).

RESULTS

All the samples studied (including XANES standards) are rhyolite glasses with FeO_T ranging from 1.0-5.7 wt%. The resulting XANES spectra show a sharp, clear pre-edge feature, with a well defined post-edge peak at ~7130 eV, followed by a deep trough at ~7160 eV and broad, shallow oscillations in the EXAFS region (figure 2). In common with Berry et al. (2003) and Wilke et al. (2005) we observe systematic changes to the shape of the spectra with increasing Fe oxidation state of the standard glasses (figure 2), including: (i) changes to the shape of the pre-edge feature, (ii) an increase in the energy of the main edge, (iii) an increase in the height and breadth (and in detail, a change in the shape) of the post-edge peak, and (iv) a slight increase in the energy of the post-edge trough. The change in energy of the post-edge trough has the potential to introduce errors into the dataset during processing if the region ~7160-7260 eV is used to normalise the spectra. We therefore normalised the spectra to the average intensity of the far post-edge region (up to 7400 eV), which avoids any of these uncertainties. Only the shape of the pre-edge feature was used to make quantitative inferences about the Fe oxidation state of the unknown samples.

The shape of the pre-edge feature is generally quantified by calculating the *centroid energy*, *C*, i.e. the area-weighted average energy of the pre-edge feature:

$$C = E_1 \frac{A_1}{A_1+A_2} + E_2 \frac{A_2}{A_1+A_2} \qquad [4]$$

where E_i is the peak energy of component *i*, and A_i is the total area (or integrated intensity) of component *i*. Average precision on the centroid energy from uncertainties in the fitting parameters is extremely good, ±0.008 eV and far better than the accuracy, which relies on calibration of the centroid energy with $Fe^{3+}/\Sigma Fe$. Fully propagated uncertainty for our analyses gave an 80% confidence interval of ~0.067 for $Fe^{3+}/\Sigma Fe$, but with very high precision. This translates to ΔfO_2 of approximately ±0.6 log units. This method assumes similar Fe coordination in the calibration standards and the unknowns because the intensities of the pre-edge components can vary with both $Fe^{3+}/\Sigma Fe$ and iron coordination (Wilke et al. 2001). All our samples have similar total pre-edge intensity (figure 3), which suggests no significant change in Fe environment and indicates an average Fe-coordination number of approximately [5], consistent with a stable mixture of [4] and [6] environments (Wilke et al. 2001) for both Fe^{2+} and Fe^{3+}. The most oxidised reference glasses plot at slightly higher total intensity than the unknowns, which may be a result of slight self-absorption effects (which has negligible effect on the centroid position, Bajt et al. 1994).

H_2O degassing

The experimentally degassed samples show a range of H_2O contents as measured by ion probe and inferred from greyscale variations (figure 4). Water contents range from 2.3 to 6.4 wt% H_2O, with one measurement at 7.2 wt% H_2O (figure 4c; table 4). These values are higher than the volatile contents as measured by FTIR (1.8 – 5.4 wt% H_2O, Mangan & Sisson 2000) but span a similar range. The cause of the discrepancy between the SIMS and FTIR data is unclear; however the key point for this study is that the glasses show clear relative variations of H_2O with $Fe^{3+}/\Sigma Fe$. Back-scattered SEM images of individual samples typically show clear increases in greyscale intensity that correlate well with decreasing H_2O concentration (figure 4b) from the core to the rim of samples with only marginal bubbles. This indicates progressive diffusive loss of H_2O to the margins of the sample to feed the growing marginal bubbles. Those samples with more vesicular interiors did not show any clear variations of BSE intensity and typically showed more limited H_2O variation.

XANES spectra for these samples have a relatively small range in pre-edge centroid energy from 7114.05 to 7114.15 eV (table 4). Total pre-edge intensity increases with increasing centroid energy (figure 3), consistent with previous observations for silicate glasses (Wilke et al. 2005). The pre-edge centroid energies for these samples correspond to an overall iron oxidation state, $Fe^{3+}/\Sigma Fe$ of 0.52 to 0.64. Although this variation is small compared to the fully propagated measurement uncertainty, there are clear relative variations both between and within samples. There is a correlation between H_2O concentration and oxidation state, consistent with an increase in $Fe^{3+}/\Sigma Fe$ due to degassing of H_2O from the melt.

Hydration

The margins of the Lipari obsidian samples are strongly hydrated, with water contents approaching the equilibrium values calculated for the experimental run conditions (4.8-5.6 wt%, Humphreys et al. 2008), while the interiors remain un-hydrated and record the initial volatile content of the Lipari obsidian starting material (~0.2 wt% H_2O; table 5). The variation in H_2O contents is clearly visible as a strong outward decreases in back-scattered SEM intensity (e.g. figure 5a; Humphreys et al. 2008). The influx of water into the samples was previously modelled successfully based on established concentration-dependent H_2O diffusivity data (Nowak & Behrens 1997; Zhang & Behrens 2000) and is consistent with H_2O diffusion into the samples over the timescale of the experiments (Humphreys et al 2008).

XANES spectra for the high-temperature hydrated samples show strong changes in pre-edge centroid energy from 7113.65 to 7114.1 eV, with one outlier at 7113.60 eV (table 5), corresponding to $Fe^{3+}/\Sigma Fe$ values from 0.04 to 0.60 (figure 5b). In marked contrast to the degassed samples, H_2O concentration correlates positively with oxidation state, indicating increasing $Fe^{3+}/\Sigma Fe$ linked to diffusion of H_2O into the sample. This is further demonstrated by the close correspondence in the shapes of the compositional profiles with distance from the margin of each chip (Figure 6). These spatial profiles also highlight a small

but apparently significant (in that it is present in each sample) negative deviation of $Fe^{3+}/\Sigma Fe$ at low H_2O contents (~0.5-1.5 wt% H_2O).

INTERPRETATION

Oxidation due to melt hydration

The hydrated samples show clearly that increasing H_2O content causes an increase in the Fe oxidation state (figures 5 and 6). This observation is very similar to the results of an earlier equilibrium study (Botcharnikov et al. 2005), which used long run times and an AuPd capsule that is permeable to H_2 to control fO_2 in the experiments, according to the equilibrium constant for the dissociation reaction:

$$H_2O\ (g) = H_2\ (g) + ½\ O_2\ (g) \qquad [5]$$

$$K_{eq}^{fl} = (fH_2 . fO_2^{1/2}) / fH_2O^{fl} \qquad [6]$$

Although fH_2 of the fluid was fixed (*via* a Shaw membrane), variations of XH_2O^{fl} between capsules introduced differences in equilibrium fO_2 in different experimental runs (Botcharnikov et al. 2005), because $fH_2O = aH_2O * f^0H_2O$ (and assuming ideal behaviour, $aH_2O \sim XH_2O$). The actual fO_2 experienced was calculated from the imposed fO_2 and XH_2O (Botcharnikov et al. 2005):

$$\log fO_2\ (\text{actual}) = \log fO_2\ (\text{imposed}) + 2 \log XH_2O \qquad [7]$$

In our experiments, we assume that the use of an Au capsule (minimally permeable to H_2 at our experimental temperatures, Chou 1986) and very short run times (20-80 minutes) resulted in approximately constant fH_2 fluid inside the experiments (see later). Our experiments were not equilibrated, and diffusion of H_2O from the fluid into the melt resulted in wide variations of XH_2O within each quenched glass chip, from water-saturated at the hydrated margin (~5.5 to 6 wt% H_2O) to highly undersaturated in the unhydrated core (~0.2 wt% H_2O). We can write equivalent reactions to [5-6] that apply for the melt phase, even though equilibration was incomplete. We therefore calculated the apparent change in $\log fO_2$ (melt) following the approach of Botcharnikov et al. (2005). We

438 assumed constant fH_2, and used either H_2O_t (the total amount of H_2O dissolved in
439 the melt) or the molecular H_2O_m (estimated from Silver et al. 1990) to calculate
440 log XH_2O_t or log XH_2O_m, i.e., $XH_2O_t = H_2O_t/H_2O_{sat}$ and $XH_2O_m = H_2Om/H_2O_{sat}$. We
441 also assumed that the marginal glass is H_2O-saturated, i.e. that $XH_2O_t = 1$ at the
442 rim, as the rim H_2O_t concentrations agree with solubility models (Humphreys et
443 al. 2008). Calculated fO_2 was converted to $Fe^{3+}/\Sigma Fe$ using the anhydrous
444 algorithm of Kress & Carmichael (1991) for the major element composition of
445 the sample and known experimental conditions. Using this approach, the overall
446 change in $Fe^{3+}/\Sigma Fe$ from core to rim in the glass samples is matched by the
447 predictions based on observed changes in XH_2O (figure 7). The lengthscale of the
448 changes in $Fe^{3+}/\Sigma Fe$ is also equivalent to the lengthscale of H_2O diffusion
449 gradients, modelled using existing H_2O_m diffusivity data (Humphreys et al. 2008),
450 demonstrating that $Fe^{3+}/\Sigma Fe$ varies at a rate controlled largely by the diffusivity
451 of H_2O_m. (figure 6). This implies that Fe oxidation state is dominated by
452 variations in XH_2O during hydration.

453 However, the shapes of the H_2O-$Fe^{3+}/\Sigma Fe$ profiles do not fit well to the
454 modelled trend (figure 7), which suggests that Fe oxidation state was only partly
455 controlled by the disequilibrium changes in XH_2O. In particular, there is a
456 significant deviation from the modelled curve to lower Fe^{3+} at low to
457 intermediate water contents (figure 7). This is in contrast to equilibrium data
458 (Botcharnikov et al. 2005), which fit the model well (figure 7). The discrepancy
459 with the equilibrium data cannot be explained by significant changes in average
460 melt Fe coordination, because the overall intensity of the pre-edge region does
461 not vary significantly with oxidation state (see figure 3; although this does not
462 preclude that coordination changes might occur).

463 Another possibility is that some 'significant' diffusion of H_2 did occur
464 across the Au capsule during the course of even these short experiments. As the
465 experiments were unbuffered it is difficult to quantify these effects but we note
466 that any H_2 loss from the capsule fluid would result in anomalously oxidised
467 sample margins, while H_2 gain would result in anomalously reduced sample
468 margins, relative to predicted values. Instead, $Fe^{3+}/\Sigma Fe$ at the sample margins is
469 well matched by the predictions – instead the unhydrated cores of the chips are

anomalously reduced relative to the predicted curves (Figure 7). Furthermore, there is no difference in profile shape between the shortest (20 minutes) and longest experiment (117 minutes), which supports our interpretation that the experiments approximately represent a closed system. There is also no difference in the width of the low-Fe^{3+} region between the shortest and longest experimental runs (figure 6). This suggests that rapid migration of H_2 preceding the H_2O diffusion front at high temperature cannot explain the discrepancy between model and observations (cf. Gaillard et al. 2002; 2003b).

Our best explanation is therefore that, although the interconversion reaction between H_2O and OH in the silicate melt is rapid at experimental temperatures (Zhang et al. 1991), reactions involving the Fe species are slower, or may involve intermediate reactions, at low H_2O contents where the melt viscosity is higher. The effect of this would be that any change in $Fe^{3+}/\Sigma Fe$ is offset to higher XH_2O in these disequilibrium experiments. This could also explain why the longer duration, equilibrium experiments of Botcharnikov et al. (2005) are more consistent with the shape of the modelled curves (see figure 7). This interpretation is consistent with the observations that relatively slow redox equilibration in metaluminous rhyolites may be linked to intermediate changes in complexing of network-modifying cations (Gaillard et al. 2003c), such as:

$$NaFe^{3+}O_2 + 2\ Si\text{-}OH = 2OH + 2Fe^{2+}_{0.5}\text{-}O\text{-}Si \qquad [8]$$

or $$H_2 + 2NaFe^{3+}O_2 + 2\ Si\text{-}O\text{-}Si = 2NaOH + 4Fe^{2+}_{0.5}OSi \qquad [9]$$

This emphasises that changes in melt oxidation state are closely linked to variations in melt chemistry and structure. Melt basicity theory may be a useful additional tool for investigation of these sorts of coupled changes than simply fO_2 measured relative to traditional oxygen buffers.

Oxidation due to H_2O degassing

The data from the experimentally degassed rhyolites are scattered but show a general trend of oxidation by ~0.5 to 1 log unit fO_2 ($Fe^{3+}/\Sigma Fe$ varies from 0.53 to 0.65) as H_2O contents decrease from ~7 to ~2 wt% (figure 4c; table 4). During decompression, the melt became H_2O-saturated and nucleated bubbles of a free

H_2O vapour phase. We infer that subsequent re-equilibration of fH_2 and fH_2O in the vapour bubble occurred through sequestration of H_2 from the melt, resulting in increased $Fe^{3+}/\Sigma Fe$ through the reaction:

$$H_2\ (g) + Fe_2O_3\ (m) = H_2O\ (m) + 2FeO\ (m) \qquad [10]$$

Although the initial fO_2 of the melt in these experiments was quite high, as a result of prolonged equilibration at high pressure in the cold seal apparatus (Mangan & Sisson 2000), this oxidation pattern is consistent with theoretical calculations of increasing oxidation state with degassing for sulphur-free melts (e.g. Mueller 1971; Candela 1986; Burgisser & Scaillet 2007). We used the approach of Burgisser et al. (2008) to simulate the change in OH partitioning between gas and melt during pressurisation in a closed system. Each pressure step results in incremental changes to the species fugacities and their concentrations in the melt, which are calculated using species solubilities, mass balance, and reaction [5]. The scale of the observed fO_2 increase is somewhat less than that predicted by the model when starting with negligible initial fluid (figure 4d). This discrepancy is unlikely to be related to significant changes in fH_2 during the course of the experiments, because the decompression run times are very short (17 to 117 minutes). Moreover, the experimental apparatus was pressurised by Ar gas, so H_2 would tend to migrate out through the capsule, decreasing fH_2 and leading to *more* oxidised conditions. Instead, it is more likely that:

(i) The modelling does not take into account the buffering capacity of FeO in the melt, which could reduce the absolute increase in oxidation state, particularly at higher initial fO_2 (Candela 1986). However, for a melt with only 1 wt% FeO (as in the case of the Panum Dome rhyolite) this should account for <0.2 log units change in fO_2 (Burgisser & Scaillet 2007).

(ii) The high proportion of fluid in the experimental capsules is buffering the changes in fO_2. The experimental starting materials include ~20 wt% fluid so there is likely to be substantial excess fluid at the beginning of each decompression run. When the modelling is repeated with 10 wt% and 20 wt% initial fluid the scale of the fO_2 increase is substantially reduced

relative to the run with 0.1 wt% initial fluid (figure 4d), consistent with the observations.

The other important difference between the experiments and the modelling is that the experiments were run without equilibration at each pressure step (Mangan & Sisson 2000); i.e., they represent disequilibrium degassing. The disequilibrium arises from delayed bubble nucleation, which is offset to lower pressure than the equilibrium case, but because they were run with a pure H_2O fluid there is no effect on the relationship between $Fe^{3+}/\Sigma Fe$ and H_2O. However, more significant kinetic factors could arise in multi-component fluids with significant differences in volatile species diffusivities. This is highlighted in experiments by Fiege et al. (2014) that showed enhanced transfer of sulphur into the fluid relative to the melt at high decompression rates, decreasing to equilibrium values with annealing and producing lower melt $Fe^{3+}/\Sigma Fe$ than predicted by equilibrium (closed-system) models.

DISCUSSION

Our data demonstrate that magma degassing and hydration can both result in significant melt oxidation coupled to changes in volatile content. On H_2O saturation, the formation of a free H_2O vapour phase partitions H_2 from the melt into the vapour and results in melt oxidation. During hydration, oxidation is caused by changes in water activity. These mechanisms should therefore be considered as one possible way to explain the high oxidation state observed in arc magmas (e.g. Carmichael 1991). Both processes have direct relevance for crustal processes and may be important in different regions of the arc crust (figure 8). Magma ascent from shallow storage regions is dominated by degassing of H_2O vapour from the melt, while rise of H_2O-undersaturated magma from the deep crust would be associated with increasing water activity. However, arc magmas are complicated by a general lack of equilibrium conditions, instead representing different components or sub-systems that may be in equilibrium at different points in the volcanic system. We therefore need to

consider what controls fO_2 and what phases would record it accurately over varying timescales.

Degassing in natural systems

Arc magma ascent through a conduit and eruption at the surface is associated with significant volatile degassing (figure 8). Our new data and modelling demonstrate that degassing of a pure or dominantly H_2O-bearing fluid results in significant melt oxidation. Under closed-system degassing conditions, this can be moderated by the presence of large volumes of gas. Furthermore, the melt can be expected to oxidise even if degassing occurs during disequilibrium degassing (delayed bubble nucleation), provided that the volatile budget is dominated by H_2O. In natural systems, we would therefore expect to observe a systematic deviation between the oxidation state of the melt relative to that of the pre-eruptive magma (as measured, for example, by 2-oxide equilibria).

Crabtree & Lange (2012) showed that bulk rock $Fe^{3+}/\Sigma Fe$ in degassed, crystal-poor andesites from the Mexican volcanic arc was within error of the pre-eruptive $Fe^{3+}/\Sigma Fe$ of the hydrous melt, as determined by 2-oxide thermobarometry. This was interpreted to mean that extensive degassing (of up to 8 wt% H_2O) during ascent had no measurable effect on magma oxidation state. Our data indicate that such strong H_2O degassing *should* leave a clear signature of oxidation in the melt phase. We therefore suggest that the magma may also have degassed additional multi-valent gas species (e.g. sulphur) that would counteract the melt oxidation driven by loss of H_2O (Burgisser et al. 2008). Alternatively, the bulk rock measurements of oxidation state in the degassed magmas may have been insufficiently sensitive to resolve any degassing effects. Direct, *in* situ measurements of melt oxidation state (e.g. by XANES) are more likely to resolve these late-stage changes.

Surface volcanic gas emissions represent the counterpart to the continuously degassing melt that is erupted (figure 8), but gas fO_2 measurements are commonly different from those of their host lavas. This has been interpreted as the result of oxidation state changes to the melt during degassing (e.g. loss of

SO_2 from basalt, Anderson & Wright 1972; Helz 2009) or mixing and integration of multi-component gases released over a range of pressures (Edmonds et al. 2010). In some cases, disequilibrium in the gas phase is evident from lack of correspondence of fO_2 estimates using different gas ratios (e.g. H_2/H_2O *cf.* CO/CO_2, Hammouya et al. 1998) and probably results from mixing of gas components with different origins, decoupled from magma ascent (Edmonds et al. 2010). In other cases the gases appear to be in equilibrium with the lavas (e.g. Gerlach 1993; Roeder et al. 2003; Gerlach 2004; Roeder et al. 2004) and the discrepancy may relate to kinetic differences in the response rate of different redox pairs (H_2-H_2O > SO_2-H_2S > CO-CO_2-CH_4, Giggenbach 1987).

These problems indicate that where multiple volatile species are present, the effects of degassing of natural arc magmas on oxidation state are complex, and strongly influenced by temperature, pressure, degassing kinetics and the initial fO_2 (Fiege et al. 2014; Burgisser & Scaillet 2007) as well as the mode of degassing (open system or closed system). This means that analysis of oxidation state during degassing of natural melts is unlikely to yield unique interpretations, although it is clear that arc magma degassing could significantly affect the oxidation state of the melt. Attaining a real understanding of the effects of magmatic degassing on oxidation state will probably require direct measurements of the concentrations and speciation of all major volatiles in the melt, as well as melt $Fe^{3+}/\Sigma Fe$ and the corresponding gas compositions.

Magma ascent from the deep crust

Recent models of arc magma genesis involve prolonged periods of deep (mafic) magma intrusion, differentiation and partial melting (e.g. Annen et al. 2006), followed by magma ascent towards upper crustal magma reservoirs where storage, degassing and mingling may also occur (Humphreys et al. 2008; Edmonds et al. 2010; Johnson et al. 2010). Our partial hydration experiments have relevance for the passage of hydrous melts or magmas between the lower crust and shallow magma storage reservoirs (figure 8). Although magmas originating from the deep crust are thought to be hydrous, they are highly unlikely to be H_2O-saturated. This means that melt aH_2O will increase during

626 ascent, as the magma gets closer to volatile saturation. By analogy with our
627 experimental results, such ascent could result in significant oxidation of the melt
628 under conditions of incomplete diffusive equilibration. Although H_2O diffusion is
629 rapid, we calculate that even in 10,000 years significant diffusion would only be
630 observed over a distance of only ~20 m at 900 °C (using the diffusivity model
631 from Nowak & Behrens 1997). This means that incomplete equilibration in
632 ascending magmas must be carefully considered as a possible source of $Fe^{3+}/\Sigma Fe$
633 heterogeneity. Moreover, this reasoning also suggests that, depending on
634 timescales, magmas in the middle to lower crust could be substantially more
635 reducing than those in the upper levels of magma storage, and hence that
636 crustal-scale variations in fO_2 may be possible at subduction zones.

637 There are already some hints of strong changes in oxidation state during
638 formation of arc magmas. For example, the cores of a population of plagioclase
639 phenocrysts in intermediate arc magmas are highly anorthitic and corroded,
640 consistent with resorption during H_2O-undersaturated magma ascent
641 (Humphreys et al. 2006). These cores may contain sulphide inclusions, indicating
642 that these plagioclase phenocrysts formed in a more reducing environment than
643 the host magmas, which are typically too oxidising to have stable sulphides. The
644 presence of Cu-Fe-sulphide inclusions in phenocrysts appears to be a relatively
645 common feature in intermediate arc magmas (e.g. Shiveluch Volcano, Kamchatka,
646 Humphreys et al. 2006; Santiaguito, Guatemala, Scott et al. 2013; Satsuma-
647 Iwojima, Japan, Ueda & Itaya 1981; Mount Pinatubo, Philippines, Pallister et al.
648 1996; and Popocatepetl, Mexico, Schaaf et al. 2005), and in their cumulates (Lee
649 et al. 2012). Sulphide crystallisation could reflect a stage of fractionation under
650 deep, more reducing, low aH_2O conditions; or alternatively may be coupled to
651 melt redox changes resulting from magnetite crystallisation (Carmichael &
652 Ghiorso 1986; Sun et al. 2004; Jenner et al. 2010), resulting in constant or
653 reducing melt $Fe^{3+}/\Sigma Fe$ but changing SO_4^{2-}/S^{2-} (Sun et al. 2004; Moretti & Papale
654 2004). In any case, these variations in oxidation state could have important
655 implications for the distribution and transport of metals within the arc crust.

656

657 **What controls fO_2 in magmatic systems?**

Although estimates of fO_2 for many magmas plot close to solid oxygen buffers (e.g. nickel - nickel oxide, NNO; or quartz-fayalite-magnetite, QFM), these phases typically do not (co)exist and it is highly unlikely that those solid buffers are controlling magma fO_2; instead they are useful reference lines in T-fO_2 space. However, it has been suggested that gas-melt redox equilibria could actually control magma fO_2, if there is abundant free vapour present in the magma. For example, Matthews et al. (1994) suggest that the sulphide-sulphate gas-phase reaction

$$SO_2\ (g) + H_2O\ (g) = H_2S\ (g) + 3/2\ O_2\ (g) \qquad [11]$$

buffered magma fO_2 at Lascar Volcano, Chile, leading to more oxidised magmas (relative to the NNO-buffer) as temperature decreases. This mechanism would require relatively sulphur-rich gases to be present, although the gas-driven buffer could be very effective because of its rapid response and large valence change (Matthews et al. 1994). The pattern of increasing divergence from oxide buffers (e.g. ΔNNO) with decreasing temperature, in a trend more parallel to the sulphide-sulphate buffer, is seen at several other volcanoes (figure 9a), including Augustine, USA (Roman et al. 2006), Shiveluch, Kamchatka (Humphreys et al. 2006), Quizapu, Chile (Ruprecht et al. 2012) and Pinatubo (Pallister et al. 1996). Data for Mount St Helens, USA as a whole lie parallel to NNO, but individual samples do not (Blundy et al. 2008), instead plotting parallel to the sulphide-sulphate buffer (figure 9a).

This suggests that sulphide-sulphate oxygen exchange between the gas and melt might be a common and effective oxygen buffering mechanism for shallowly stored magmas. However, the arrays of T-fO_2 points from coexisting oxide compositions are also parallel to isopleths of constant hm/ilm (taken from Buddington & Lindsley 1964; figure 9b). Isopleths of constant mt/üsp in titanomagnetite are at a slightly steeper angle (figure 9b). Therefore, the oxide data could also be explained by increased temperature causing increasing üsp content while hm/ilm remains constant. This is consistent with the slower diffusion rates in ilm-hm solid solution than in mt-üsp (Hammond & Taylor 1982). A simpler interpretation for these T-fO_2 trends is therefore that late-stage heating has resulted in a diffusive increase in üsp-content of titanomagnetites,

690 while adjustment of ilmenite compositions is kinetically inhibited. The increased
691 temperature could be due to release of latent heat of crystallisation (Blundy et al.
692 2006) or to mingling with hotter magmas (e.g. Devine et al. 2003; Ruprecht et al.
693 2012). This is consistent with compositional variations in oxides from Soufrière
694 Hills Volcano, Montserrat (figure 9b; data from Devine et al. 2003). Ilmenites are
695 uniform, while titanomagnetites have zoned rims with high TiO_2 due to magma
696 mixing (Devine et al. 2003). The apparent T-fO_2 data plot along hm-ilm isopleths
697 and lie parallel to the sulphide-sulphate buffer (figure 9b). Demonstrating fO_2
698 control by gas-melt equilibria such as [11] would require evidence of constant
699 melt redox ratios for the redox couple of interest, probably through analysis of
700 suites of melt inclusions.

701 Disequilibrium between crystals and melt is a ubiquitous feature of
702 shallow crustal arc magma storage: arc magmas typically comprise components
703 or sub-systems that may be only in equilibrium at certain points in the volcanic
704 system (e.g. Pichavant et al. 2007). For minerals, equilibration timescales are
705 poorly known but probably slow, except for Fe-Ti oxides, which may equilibrate
706 relatively quickly (i.e., < 5 years at 900 °C for complete equilibration of a 250 μm
707 oxide phenocryst, Freer & Hauptman 1978). This means that fO_2 calculated from
708 solid-melt equilibria involving homogeneous Fe-Ti oxide phenocrysts (± H_2O)
709 should be an accurate record (sensor) of stable magma storage conditions in the
710 shallow system. However, oxides will probably not provide a good record of
711 earlier or longer-term changes in fO_2 during fractionation, nor of late-stage
712 changes during magma ascent. Instead, more slowly equilibrating phenocrysts
713 such as pyroxene or hornblende, or oxides brought rapidly to the surface in
714 cumulate nodules, may be more useful as a record of longer term changes;
715 whereas melt redox couples will be needed to investigate variations immediately
716 prior to eruption.

717

718

719 **SUMMARY**

Direct measurement of coupled changes in melt $Fe^{3+}/\Sigma Fe$ and H_2O content in partially hydrated and degassed experimental rhyolites confirms that significant changes in oxidation state can occur in response to changes in volatile content. During hydration, increases in aH_2O produced strong melt oxidation. This suggests that ascent of H_2O-undersaturated arc magmas from the deep crust could cause significant oxidation, depending on the timescales required for equilibration relative to magma storage times. During degassing, oxidation arises due to loss of H_2 together with H_2O, consistent with theoretical modelling for H_2O fluids. It is therefore possible that significant vertical variations in magma oxidation state may develop within the arc crust. During the fractionation, storage and ascent of natural arc magmas, the controls on fO_2 may be expected to vary depending on the nature and duration of magma storage, as well as kinetic factors and the timescales of observation and equilibration. The differing response times of possible oxygen buffers and/or fO_2 sensors (such as oxide pairs) need to be considered alongside the degree of attainment of equilibrium in the magma. It is clear that attaining a real understanding of the effects of magmatic degassing on oxidation state will probably require direct measurements of the concentrations and speciation of all major volatiles in the melt, as well as melt $Fe^{3+}/\Sigma Fe$ and the corresponding gas compositions. In this respect, melt structure and chemistry should be considered alongside variations of fO_2 relative to traditional buffers.

ACKNOWLEDGEMENTS

We acknowledge facilities grants from DIAMOND Light Source (SP6681 and SP8203) and the NERC ion microprobe facility (IMF452), and thank Tina Geraki, Konstantin Ignatyev and Cees Jan de Hoog for expert analytical assistance. We acknowledge Iris Buisman for assistance with electron microprobe analysis, and Mike Stock, David Pyle and, in particular, Victoria Smith for assistance during synchrotron beamtime. We are grateful to Liz Cottrell for useful discussions and for the loan of reference materials from the Department of Mineral Sciences, Smithsonian Institution (NMNH117393). We acknowledge useful discussions with Andrew Matzen, Bernie Wood, James Tuff and Jon Wade. The manuscript

was improved by helpful and insightful reviews from Richard Arculus, Cin-Ty Lee and an anonymous reviewer, as well as helpful comments from Tom Sisson and Marie Edmonds, and careful editorial input from Marjorie Wilson. MCSH is supported by a Royal Society University Research Fellowship, and RAB is funded by ERC grant 'Critmag'.

REFERENCES

Anderson, A.T. & Wright, T.L.W. (1972) Phenocrysts and glass inclusions and their bearing on oxidation and mixing of basaltic magmas, Kilauea volcano, Hawaii. *American Mineralogist* **57**, 188-216

Annen, C., Blundy, J.D. & Sparks, R.S.J. (2006) The genesis of intermediate and silicic magmas in deep crustal hot zones. *Journal of Petrology* **47**, 505-539

Ballhaus (1993) Redox states of lithospheric and asthenospheric upper mantle. *Contributions to Mineralogy and Petrology* **114**, 331-348

Berry, A.J., O'Neill, H., Jayasuriya, K.D., Campbell, S.J. & Foran, G.J. (2003) XANES calibrations for the oxidation state of iron in a silicate glass. A*merican Mineralogist* **88**, 967-977

Blundy, J. & Cashman, K. (2005) Rapid decompression-driven crystallization recorded by melt inclusions from Mount St Helens volcano. *Geology* **33**, 793-796

Blundy, J., Cashman, K. & Humphreys, M. (2006) Magma heating by decompression-driven crystallization beneath andesite volcanoes. *Nature* **443**, 76-80

Blundy, J., Cashman, K.V. & Berlo, K. (2008) Evolving magma storage conditions beneath Mount St Helens inferred from chemical variations in melt inclusions from the 1980-1986 and current (2004-2006) eruptions. *In:* A volcano rekindled: The renewed eruption of Mount St. Helens, 2004-2006. *USGS Professional Paper* **1750**

Botcharnikov, R.E., Koepke, J., Holtz, F., McCammon, C. & Wilke, M. (2005) The effect of water activity on the oxidation and structural state of Fe in a ferro-basaltic melt. *Geochimica et Cosmochimica Acta* **69**, 5071-5085

782 Brandon, A.D. & Draper, D.S. (1996) Constraints on the origin of the oxidation
783 state of mantle overlying subduction zones: An example from Simcoe,
784 Washington, USA. *Geochimica et Cosmochimica Acta* **60**, 1739-1749

785 Brooker, R.A., Kohn, S.C., Holloway, J.R., McMillan, P.F. & Carroll, M.R. (1999)
786 Solubility, speciation and dissolution mechanisms for CO_2 in melts on the
787 $NaAlO_2$-SiO_2 join. *Geochimica et Cosmochimica Acta* **63**, 3549-3565

788 Buddington, A.F. & Lindsley, D.H. (1964) Iron-Titanium oxide minerals and
789 synthetic equivalents. *Journal of Petrology* **5**, 310-357

790 Burgisser, A. & Scaillet, B. (2007) Redox evolution of a degassing magma rising to
791 the surface. *Nature* **445**, 194-197

792 Burgisser, A., Scaillet, B. & Harshvardhan (2008) Chemical patterns of erupting
793 silicic magmas and their influence on the amount of degassing during ascent.
794 *Journal of Geophysical Research* **113**, B12204

795 Burnham, C.W. (1975) Water and magmas; a mixing model. *Geochimica et*
796 *Cosmochimica Acta* **39**, 1077-1084

797 Candela, P.A. (1986) The evolution of aqueous vapor from silicate melts: Effect
798 on oxygen fugacity. *Geochimica et Cosmochimica Acta* **50**, 1205-1211

799 Carmichael, I.S.E. (1991) The redox states of basic and silicic magmas: a
800 reflection of their source regions? *Contributions to Mineralogy and Petrology* **106**,
801 129-141

802 Carmichael, I.S.E. & Ghiorso, M.S. (1986) Oxidation-reduction relations in basic
803 magma: a case for homogeneous equilibria. *Earth and Planetary Science Letters*
804 **78**, 200-210

805 Cottrell, E., Kelley, K.A., Lanzirotti, A. & Fischer, R.A. (2009) High-precision
806 determination of iron oxidation state in silicate glasses using XANES. C*hemical*
807 *Geology* **268**, 167-179

808 Crabtree, S.M. & Lange, R.A. (2012) An evaluation of the effect of degassing on the
809 oxidation state of hydrous andesite and dacite magmas: a comparison of pre- and
810 post-eruptive Fe^{2+} concentrations. *Contributions to Mineralogy and Petrology*
811 **163**, 209-224

812 Devine, J.D., Rutherford, M.J., Norton, G.E. & Young, S.R. (2003). Magma storage
813 region processes inferred from geochemistry of Fe-Ti oxides in andesitic magma,
814 Soufrière Hills Volcano, Montserrat, W.I. *Journal of Petrology* **44**, 1375-1400

815 Duffy, J.A. (1993) A review of optical basicity and its applications to oxidic
816 systems. *Geochimica et Cosmochimica Acta* **57**, 3961-3970

817 Edmonds, M., Aiuppa, A., Humphreys, M., Moretti, R., Giudice, G., Martin, R.S.,
818 Herd, R.A. & Christopher, T. (2010) Excess volatiles supplied by mingling of mafic
819 magma at an andesite arc volcano. *G-cubed*, **11**, Q04005

820 Evans, K.A., Elburg, M.A. & Kamenetsky, V.S. (2012) Oxidation state of subarc
821 mantle. *Geology*, doi:10.1130/G33037.1

822 Fiege, A., Behrens, H., Holtz, F. & Adams, F. (2014) Kinetic vs. thermodynamic
823 control of degassing of H_2O-S±Cl-bearing andesitic melts. *Geochimica et*
824 *Cosmochimica Acta* **125**, 241-264

825 Flood, H. & Förland, T. (1947) The acidic and basic properties of oxides. *Acta*
826 *Chemica Scandinavica* **1**, 592-604

827 Fraser, D.G. (1975) Activities of trace elements in silicate melts. *Geochimica et*
828 *Cosmochimica Acta* **39**, 1525-1530

829 Fraser, D.G. (1977) Thermodynamic properties of silicate melts. *In:*
830 Thermodynamics in Geology, edited by D.G. Fraser (D. Reidel Pub. Co.,
831 Dordrecht), p303-325.

832 Fraser, D.G. (2005) Acid-base properties and structons: towards a structural
833 model for predicting the thermodynamic properties of silicate melts. *Annals of*
834 *Geophysics* **48**, 549-559

835 Freer, R. & Hauptman, Z. (1978) An experimental study of magnetite-
836 titanomagnetite interdiffusion. *Physics of the Earth and Planetary Interiors* **16**,
837 223-231

838 Frost, D.J. & McCammon, C.A. (2008) The redox state of Earth's mantle. *Annual*
839 *Review of Earth & Planetary Sciences* **36**, 389-420

840 Gaillard, F., Scaillet, B., Pichavant, M. & Bény, J.-M. (2001) The effect of water and
841 fO_2 on the ferric-ferrous ratio of silicic melts. *Chemical Geology* **174**, 255-273

842 Gaillard, F., Scaillet, B. & Pichavant, M. (2002) Kinetics of iron oxidation-
843 reduction in hydrous silicic melts. *American Mineralogist* **87**, 829-837

844 Gaillard, F., Pichavant, M. & Scaillet, B. (2003a) Experimental determination of
845 activities of FeO and Fe_2O_3 components in hydrous silicic melts under oxidising
846 conditions. *Geochimica et Cosmochimica Acta* **67**, 4389-4409

847 Gaillard, F., Schmidt, B., Mackwell, S. & McCammon, C. (2003b) Rate of hydrogen-
848 iron redox exchange in silicate melts and glasses. *Geochimica et Cosmochimica*
849 *Acta* **67**, 2427-2441

850 Gaillard, F., Pichavant, M., Mackwell, S., Champallier, R., Scaillet, B. & McCammon,
851 C. (2003c) Chemical transfer during redox exchanges between H_2 and Fe-bearing
852 silicate melts. *American Mineralogist* **88**, 308-315

853 Gerlach, T.M. (1993) Oxygen buffering of Kilauea volcanic gases and the oxygen
854 fugacity of Kilauea basalt. *Geochimica et Cosmochimica Acta* **57**, 795-814

855 Gerlach, T.M. (2004) Comment on paper: 'Morphology and compositions of
856 spinel in Pu'u 'O'o lava (1996-1980, Kilauea volcano, Hawaii' – enigmatic
857 discrepancies between lava and gas-based fO_2 determinations of Pu'u 'O'o lava.
858 *Journal of Volcanology and Geothermal Research* **134**, 241-244

859 Ghiorso & Sack (1991) Fe-Ti oxide geothermometry: thermodynamic
860 formulation and the estimation of intensive variables in silicic magmas.
861 *Contributions to Mineralogy and Petrology* **108**, 485-510

862 Giggenbach, W.F. (1996) Redox processes governing the chemistry of fumarolic
863 gas discharges from White Island, New Zealand. *Applied Geochemistry* **2**, 143-161

864 Hammond, P.A. & Taylor, L.A. (1982) The ilmenite/ titano-magnetite assemblage:
865 kinetics of re-equilibration. *Earth and Planetary Science Letters* **61**, 143-150

866 Hammouya, G., Allard, P., Jean-Baptiste, P., Parello, F., Semet, M.P. & Young, S.R.
867 (1998) Pre- and syn-eruptive geochemistry of volcanic gases from Soufriere Hills
868 of Montserrat, West Indies. *Geophysical Research Letters* **25**, 3685-3688

869 Helz, R.T. (2009) Reduction of basaltic melt during near-surface evolution of SO_2:
870 A possible example from Kilaeua. *Portland GSA Annual Meeting,* 2009.

871 Humphreys, M.C.S., Kearns, S.L. & Blundy, J.D. (2006a) SIMS investigation of
872 electron-beam damage to hydrous, rhyolitic glasses: Implications for melt
873 inclusion analysis. *American Mineralogist* **91**, 667-679

874 Humphreys, M.C.S., Blundy, J.D. & Sparks, R.S.J. (2006b) Magma evolution and
875 open-system processes at Shiveluch Volcano: Insights from phenocryst zoning.
876 *Journal of Petrology* **47**, 2303-2334

877 Humphreys, M.C.S., Menand, T., Blundy, J.D. & Klimm, K. (2008) Magma ascent
878 rates in explosive eruptions: constraints from H_2O diffusion in melt inclusions.
879 *Earth and Planetary Science Letters* **270**, 25-40

880 Jenner, F.E., O'Neill, H.St C., Arculus, R.J. & Mavrogenes, J.A. (2010) The magnetite
881 crisis in the evolution of arc-related magmas and the initial concentration of Au,
882 Ag and Cu. *Journal of Petrology* **51**, 2445-2464

883 Johnson et al. (2010) Degassing of volatiles (H_2O, CO_2, S, Cl) during ascent,
884 crystallization and eruption at mafic monogenetic volcanoes in central Mexico.
885 *Journal of Volcanology and Geothermal Research* **197**, 225-238

886 Kelley, K.A. & Cottrell, E. (2009) Water and the oxidation state of subduction
887 zone magmas. *Science* **325**, 605-607

888 Kress & Carmichael (1991) The compressibility of silicate liquids containing
889 Fe_2O_3 and the effect of composition, temperature, oxygen fugacity and pressure
890 on their redox states. *Contributions to Mineralogy and Petrology* **108**, 82-92

891 Kushiro, I. (1975) On the nature of silicate melt and its significance in magma
892 genesis: regularities in the shift of the liquidus boundaries involving olivine,
893 pyroxene, and silica minerals. *American Journal of Science* **275**, 411-431

894 Lecuyer, C. & Ricard, Y. (1999) Long-term fluxes and budget of ferric iron:
895 implication for the redox states of the Earth's mantle and atmosphere. *Earth and*
896 *Planetary Science Letters* **165**, 197-211

897 Lee C-T.A., Luffi, P., Le Roux, V., Dasgupta, R., Albarede, F. & Leeman, W.P. (2010)
898 The redox state of arc mantle using Zn/Fe systematics. *Nature* **468**, 681-685

899 Lee, C-T.A., Luffi, P., Chin, E.J., Bouchet, R., Dasgupta, R., Morton, D.M., Le Roux, V.,
900 Yin, Q. & Jin, D. (2012) Copper systematics in arc magmas and implications for
901 crust-mantle differentiation. *Science* **336**, 64-68

902 Mallman, G. & O'Neill, H. (2009) The crystal/melt partitioning of V during mantle
903 melting as a function of oxygen fugacity compared with some other elements (Al,
904 P, Ca, Sc, Ti, Cr, Fe, Ga, Y, Zr and Nb). *Journal of Petrology* **50**, 1765-1794

905 Mangan, M. & Sisson, T. (2000) Delayed, disequilibrium degassing in rhyolite
906 magma: decompression experiments and implications for explosive volcanism.
907 *Earth and Planetary Science Letters* **183**, 441-455

908 Mathez, E.A. (1984) Influence of degassing on oxidation states of basaltic
909 magmas. *Nature* **310**, 371-375

910 Matthews, S.J., Jones, A.P. & Beard, A.D. (1994) Buffering of melt oxygen fugacity
911 by sulphur redox reactions in calc-alkaline magmas. *Journal of the Geological*
912 *Society, London* **151**, 815-823

913 Moore, G., Righter, K. & Carmichael, I.S.E. (1995) The effect of dissolved water on
914 the oxidation state of iron in natural silicate liquids. *Contributions to Mineralogy*
915 *and Petrology* **120**, 170-179

916 Moretti, R. (2005) Polymerisation, basicity, oxidation state and their role in ionic
917 modelling of silicate melts. *Annals of Geophysics* **48**, 583-608

918 Moretti, R. & Papale, P. (2004) On the oxidation state and volatile behaviour in
919 multicomponent gas-melt equilibria. *Chemical Geology* **213**, 265-280

920 Morris, R.V. & Haskin, L.A. (1974) EPR measurement of the effect of glass
921 composition on the oxidation states of europium. *Geochimica et Cosmochimica*
922 *Acta* **38**, 1435-1445

923 Mueller, R.F. (1971) Oxidative capacity of magmatic components. *American*
924 *Journal of Science* **270**, 236-243

925 Mysen, B.O., Kumamoto, K., Cody, G.D. & Fogel, M.L. (2011). Solubility and
926 solution mechanisms of C-O-H volatiles in silicate melt with variable redox
927 conditions and melt composition at upper mantle temperatures and pressures.
928 *Geochimica et Cosmochimica Acta* **75**, 6183-6199

929 Nowak, M. & Behrens, H. (1997) An experimental investigation on diffusion of
930 water in haplogranitic melts. *Contributions to Mineralogy and Petrology* **126**,
931 365-376

932 Ottonello, G., Moretti, R., Marini, L. & Vetuschi Zuccolini, M. (2001) Oxidation
933 state of iron in silicate glasses and melts: a thermochemical model. Ch*emical*
934 *Geology* **174**, 157-179

935 Pallister, J.S., Hoblitt, R.P., Meeker, G.P., Knight, R.J. & Siems, D.F. (1996) Magma
936 mixing at Mount Pinatubo: Petrographic and chemical evidence from the 1991
937 deposits. *In:* Fire and Mud: Eruptions and Lahars of Mount Pinatubo, Philippines

938 Parkinson, I.J. & Arculus, R.J. (1999) The redox state of subduction zones:
939 insights from arc-peridotites. *Chemical Geology* **160**, 409-423

940 Paul & Douglas (1965) Ferrous-ferric equilibrium in binary alkali silicate glasses.
941 *Physics and Chemistry of Glasses* **6**, 207-211

942 Ravel, B. & Newville, M. (2005). ATHENA, ARTEMIS, HEPHAESTUS: data analysis
943 for X-ray absorption spectroscopy using IFEFFIT. *Journal of Synchrotron*
944 *Radiation* **12**, 537-541

945 Roeder, P.L., Thornber, C., Poustovetov, A. & Grant, A. (2003) Morphology and
946 composition of spinel in Pu'u O'o lava (196-1998), Kilauea volcano, Hawaii.
947 *Journal of Volcanology and Geothermal Research* **123**, 245-265

948 Roeder, P.L., Thornber, C. & Grant, A. (2004) Reply to comment on paper:
949 'Morphology and composition of spinel in Pu'u O'o lava (196-1998), Kilauea
950 volcano, Hawaii' – enigmatic discrepancies between lava and gas-based fO_2
951 determinations of Pu'u O'o lava. *Journal of Volcanology and Geothermal Research*
952 **134**, 245-248

953 Ruprecht, P., Bergantz, G.W., Cooper, K.M. & Hildreth, W. (2012) The crustal
954 magma storage system of Volcàn Quizapu, Chile, and the effects of magma mixing
955 on magma diversity. *Journal of Petrology* **53**, 801-840

956 Sack, R.O., Carmichael, I.S.E., Rivers, M. & Ghiorso, M.S. (1980) Ferric-ferrous
957 equilibria in natural silicate liquids at 1 bar. *Contributions to Mineralogy and*
958 *Petrology* **75**, 369-376

959 Sato, M. (1978) Oxygen fugacity of basaltic magmas and the role of gas-forming
960 elements. *Geophysical Research Letters* **5**, 447-449

961 Schuessler, J.A., Botcharnikov, R.E., Behrens, H., Misiti, V. & Freda, C. (2008)
962 Oxidation state of iron in hydrous phono-tephritic melts. *American Mineralogist*
963 **93**, 1493-1504

964 Silver, L., Ihinger, P.D. & Stolper, E. (1990) The influence of bulk composition on
965 the speciation of water in silicate glasses. *Contributions to Mineralogy and*
966 *Petrology* **104**, 142-162

967 Sisson, T.W. & Grove, T.L. (1993) Experimental investigations of the role of H_2O
968 in calc-alkaline differentiation and subduction zone magmatism. *Contributions to*
969 *Mineralogy and Petrology* **113**, 143-166

970 Stolper, E. (1982) The speciation of water in silicate melts. *Geochimica et*
971 *Cosmochimica Acta* **46**, 2609-2620

972 Sun, W., Arculus, R.J., Kamenetsky, V.S. & Binns, R.A. (2004) Release of gold-
973 bearing fluids in convergent margin magmas prompted by magnetite
974 crystallization. *Nature* **431**, 975-978

975 Tilquin, J.-Y., Duveiller, P., Glibert, J. & Claes, P. (1997) Effect of basicity on redox
976 equilibria in sodium silicate melts: An in situ electrochemical investigation.
977 *Journal of Non-Crystalline Solids* **211**, 95-104

978 Toop, G.W. & Samis, C.S. (1962) Activities of ions in silicate melt. *Transactions of*
979 *the Metallurgical Society* **224**, 878-887

980 Toplis, M.J. (2005) The thermodynamics of iron and magnesium partitioning
981 between olivine and liquid: criteria for assessing and predicting equilibrium in
982 natural and experimental systems. *Contributions to Mineralogy and Petrology*
983 **149**, 22-39

984 Wilke, M., Farges, F., Petit, P.-E., Brown, G.E. & Martin, F. (2001) Oxidation state
985 and coordination of Fe in minerals: An Fe K-XANES spectroscopic study.
986 *American Mineralogist* **86**, 714-730

Wilke, M., Partzsch, G.M., Bernhardt, R. & Lattard, D. (2005) Determination of the iron oxidation state in basaltic glasses using XANES at the K-edge. Ch*emical Geology* **220**, 143-161

Wood, B.J., Bryndzia, L.T. & Johnson, K.E. (1990) Mantle oxidation state and its relationship to tectonic environment and fluid speciation. *Science* **248**, 337-345

Xue, X. & Kanzaki, M. (2004) Dissolution mechanisms of water in depolymerized silicate melts: Constraints from ^{1}H and ^{29}Si NMR spectroscopy and ab initio calculations. *Geochimica et Cosmochimica Acta* **68**, 5027-5057

Xue, X. & Kanzaki, M. (2006) Depolymerization effect of water in aluminosilicate glasses: Direct evidence from ^{1}H-^{27}Al heteronuclear correlation NMR. *American Mineralogist* **91**, 1922-1926

Yokokawa, T. (1986) Gas solubilities in molten salts and silicates. *Pure and Applied Chemistry* **58**, 1547-1552

Zhang, Y., Stolper, E.M. & Wasserburg, G.J. (1991) Diffusion of water in rhyolitic glasses. *Geochimica et Cosmochimica Acta* **55**, 441-456

Zhang, Y. & Behrens, H. (2000) H_2O diffusion in rhyolitic melts and glasses. *Chemical Geology* **169**, 243-262

FIGURES

Figure1

Calibration lines for determining $Fe^{3+}/\Sigma Fe$ from XANES centroid energy (a) and H_2O from $^{1}H^{+}/^{30}Si^{+}$ ion probe measurements (b). In (a) errors in $Fe^{3+}/\Sigma Fe$ are derived from Mossbauer spectroscopy (Cottrell et al. 2009) while uncertainties in centroid energy are equivalent to the fitting uncertainty. Data are presented as linear deviation of centroid energy from 7113.6 eV, to facilitate regression. Solid line: best fit linear regression. Dashed lines: fully propagated uncertainties at 80% confidence limits based on the linear regression. (b) Typical daily ion microprobe calibration curve for $^{1}H^{+}/^{30}Si^{+}$ *vs* H_2O showing best fit linear regression (solid line) and upper and lower 95% confidence limits (dashed

lines). Uncertainties in H_2O are the errors on independently measured H_2O contents of the standard glasses.

Figure 2

a) Typical normalised, background-corrected XANES spectrum for rhyolite standard glass. Boxes show parts of the spectrum that show variations with oxidation state. b) The pre-edge region shows two peaks; the relative importance of the higher-energy peak increases with increasing $Fe^{3+}/\Sigma Fe$. Each spectrum is offset by 0.02 on the y-axis. c) The energy of the main edge increases systematically with increasing $Fe^{3+}/\Sigma Fe$ (spectra are not offset). d) The energy of the peak and post-edge trough increases with $Fe^{3+}/\Sigma Fe$, though higher energy resolution in this region is needed to use this feature quantitatively. Each spectrum is offset by 0.02 on the y-axis. NB. Where additional symbol markers are used, these represent every fifth data point.

Figure 3

Total pre-edge intensity plotted against pre-edge centroid energy, after Wilke et al. (2005). Light grey dots and dashed curves represent Fe coordination end-member positions and mixing lines derived from Wilke et al. (2005). Triangles – rhyolite glass standards, Cottrell et al. (2009). Squares: partially hydrated Lipari rhyolite. Circles: high-temperature degassed rhyolites from Mangan & Sisson (2000). Solid grey curve represents the range of standard glasses presented by Wilke et al. (2005).

Figure 4

a) Backscattered electron SEM images of representative glass chips from Mangan & Sisson (2000), in which heterogeneous bubble nucleation at the margins of the chips was dominant. Scale bar is 1mm. Lower greyscale intensity in the core indicates higher water contents, as demonstrated by the negative linear correlation between greyscale and H_2O (b). Degassing of H_2O is associated with

1046 increasing $Fe^{3+}/\Sigma Fe$ (c) and fO_2 relative to the Nickel-Nickel oxide buffer (d).
1047 Errors in (c) relate to ~10% uncertainty in H_2O and 80% confidence limits for
1048 $Fe^{3+}/\Sigma Fe$. Note that the analytical *precision* is smaller than the size of the
1049 individual points. Modelled trends in (d) are theoretical predictions for
1050 degassing of S-free rhyolite following Burgisser et al. (2008), starting at different
1051 initial fO_2 and with no free fluid (0.1 wt% initial gas, red line) or with 10 wt%
1052 (green) or 20 wt% (black) initial fluid.

1053

1054 Figure 5

1055 Backscattered electron SEM image showing variation of greyscale intensity
1056 related to inward diffusion of H_2O into the Lipari glass chips at high temperature
1057 (a), reproduced from Humphreys et al. (2008). (b) Co-variation of $Fe^{3+}/\Sigma Fe$ with
1058 H_2O content and equivalent fO_2 variation relative to the NNO buffer.
1059 Representative error bars shown for sample LIPRF5.

1060

1061 Figure 6

1062 Spatial variability of $Fe^{3+}/\Sigma Fe$ (grey squares) and H_2O (black triangles) with
1063 distance from the margin of each chip hydrated at high temperature. $Fe^{3+}/\Sigma Fe$ in
1064 the un-hydrated starting material is marked by a grey band in each figure.
1065 Horizontal error bars in (a) are the estimated maximum uncertainty on spatial
1066 location of each point. Errors in $Fe^{3+}/\Sigma Fe$ and H_2O are reported in previous
1067 figures.

1068

1069 Figure 7

1070 Variation of $Fe^{3+}/\Sigma Fe$ and H_2O within experimentally hydrated glass chips
1071 (squares). Modelled variation of $Fe^{3+}/\Sigma Fe$ based on changing water activity is
1072 shown by the bold lines (calculated from XH_2O_m) and dashed lines (calculated
1073 from XH_2Ot). Calculated variations for two different illustrative initial fO_2
1074 conditions are shown (black and grey lines and labels).

1075

1076 Figure 8

1077 Schematic figure showing the possible variations in importance of possible
1078 different fO_2 control mechanisms in different parts of the volcanic system and
1079 crust, depending on kinetics and degree of equilibration. See text for discussion.

1080

1081 Figure 9

1082 Temperature-fO_2 variations in intermediate arc magmas (a). Different oxygen
1083 buffers are shown in bold black lines (constant sulphide-sulphate ratios) and
1084 grey dashed lines (NNO, NNO+1). Data points are from two-oxide equilibria. Data
1085 sources are Blundy et al (2008) for Mount St Helens, USA; Humphreys et al.
1086 (2006) for Shiveluch Volcano, Kamchatka; Roman et al. (2006) for Augustine,
1087 Aleutians; Crabtree & Lange (2012) for the Mexican arc; Murphy et al. (2000) for
1088 Soufriere Hills, Montserrat; Sparks et al. (2008) for Uturuncu Volcano, Bolivia;
1089 Pallister et al. (1996) for Mount Pinatubo, Philippines; and Matthews et al.
1090 (1994) for Lascar Volcano, Chile. The pale grey arrow shows the data trend from
1091 part (b), which also shows isopleths (thin grey lines) of constant hm-ilm and
1092 Usp-mt composition from Buddington & Lindsley (1969). Black circles in (b) are
1093 data on zoned magnetite grains from Soufrière Hills Volcano, Montserrat (from
1094 Devine et al. 2003) which plot along lines of constant hm-ilm and also lie parallel
1095 to the sulphide-sulphate buffer.

1096

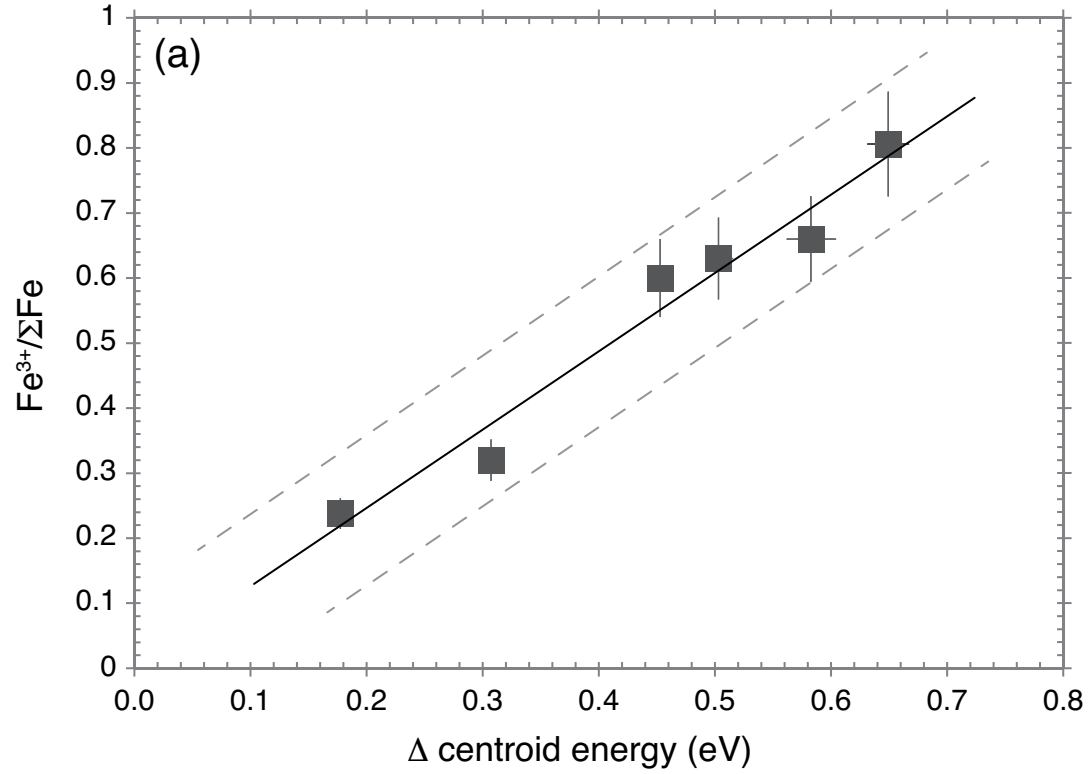
(a)
Fe3+/ΣFe
Δ centroid energy (eV)
0
0.1
0.2
0.3
0.4
0.5
0.6
0.7
0.8
0.9
1
0.0
0.1
0.2
0.3
0.4
0.5
0.6
0.7
0.8

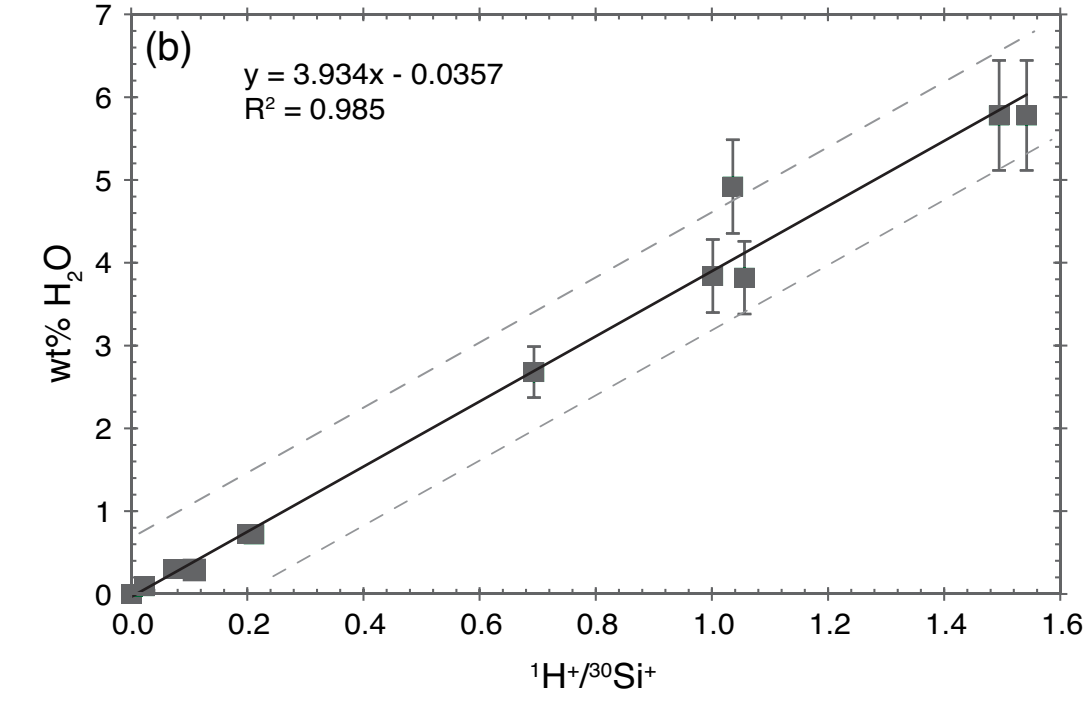
(b)
y = 3.934x - 0.0357
R² = 0.985
wt% H2O
1H+/30Si+
0
1
2
3
4
5
6
7
0.0
0.2
0.4
0.6
0.8
1.0
1.2
1.4
1.6

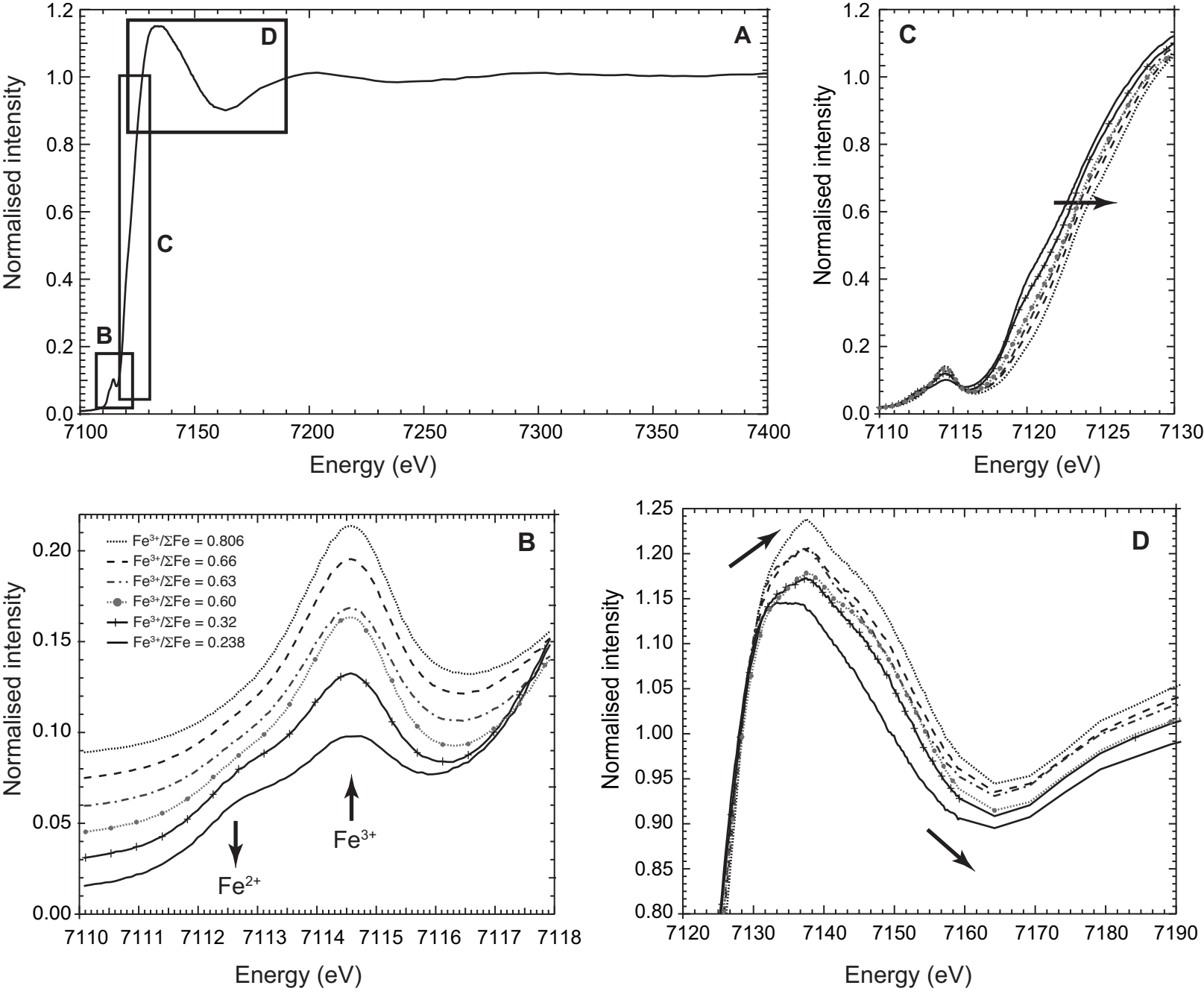
A
B
C
D
Normalised intensity
Energy (eV)
Fe³⁺/ΣFe = 0.806
Fe³⁺/ΣFe = 0.66
Fe³⁺/ΣFe = 0.63
Fe³⁺/ΣFe = 0.60
Fe³⁺/ΣFe = 0.32
Fe³⁺/ΣFe = 0.238
Fe²⁺
Fe³⁺

Figure 2

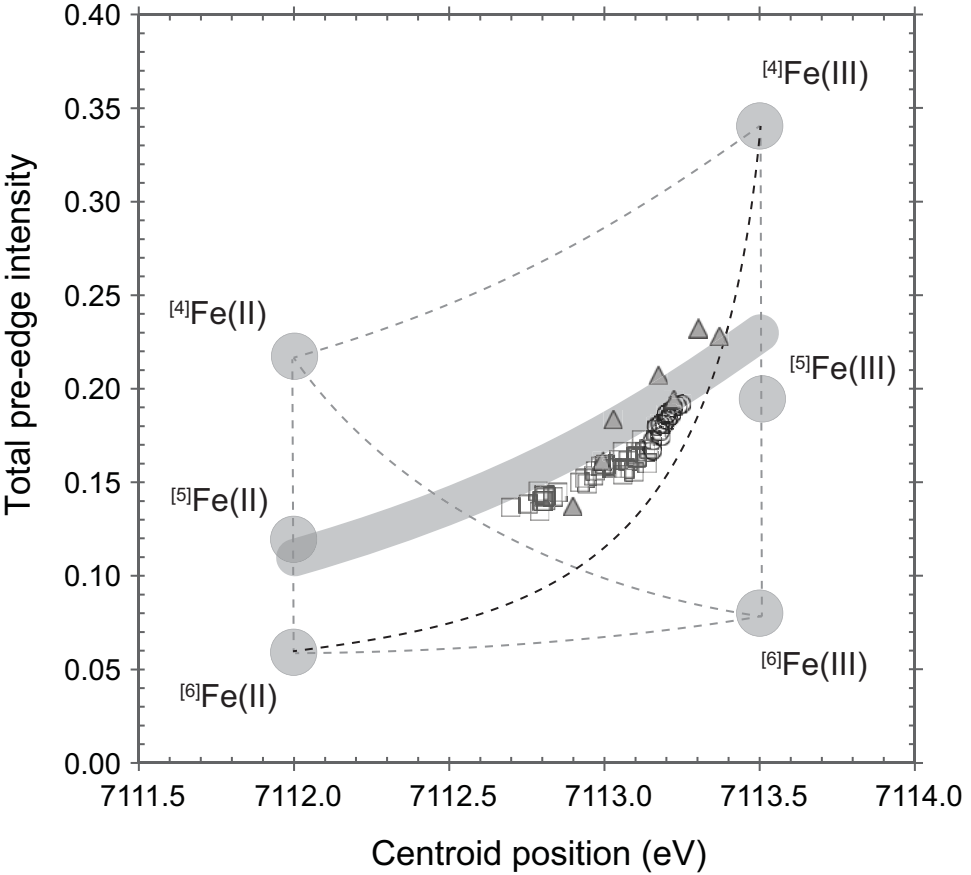
Total pre-edge intensity
0.40
0.35
0.30
0.25
0.20
0.15
0.10
0.05
0.00
7111.5
7112.0
7112.5
7113.0
7113.5
7114.0
Centroid position (eV)
[4]Fe(III)
[4]Fe(II)
[5]Fe(III)
[5]Fe(II)
[6]Fe(III)
[6]Fe(II)

Figure 3

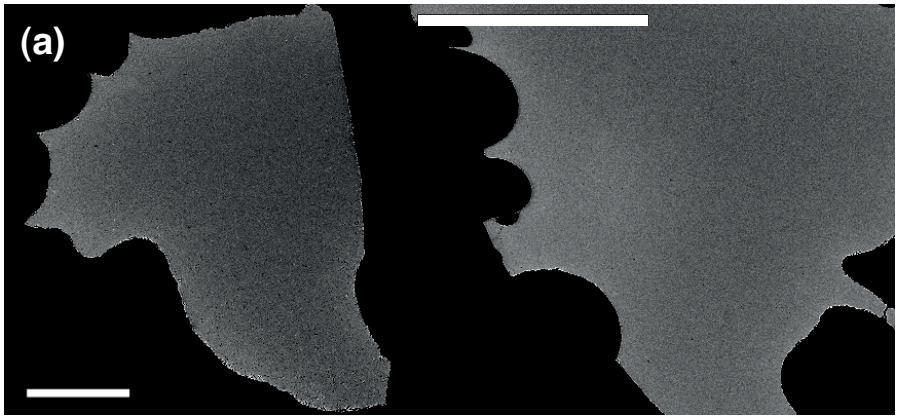
(a)

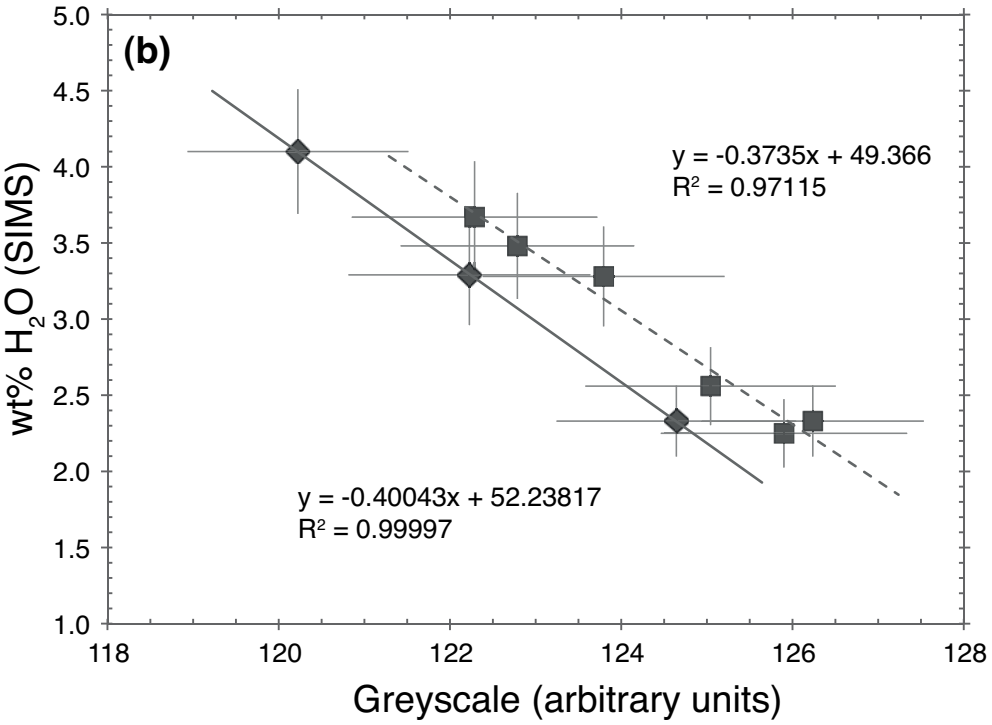
(b)
y = -0.3735x + 49.366
R² = 0.97115
y = -0.40043x + 52.23817
R² = 0.99997
wt% H2O (SIMS)
Greyscale (arbitrary units)
5.0
4.5
4.0
3.5
3.0
2.5
2.0
1.5
1.0
118
120
122
124
126
128

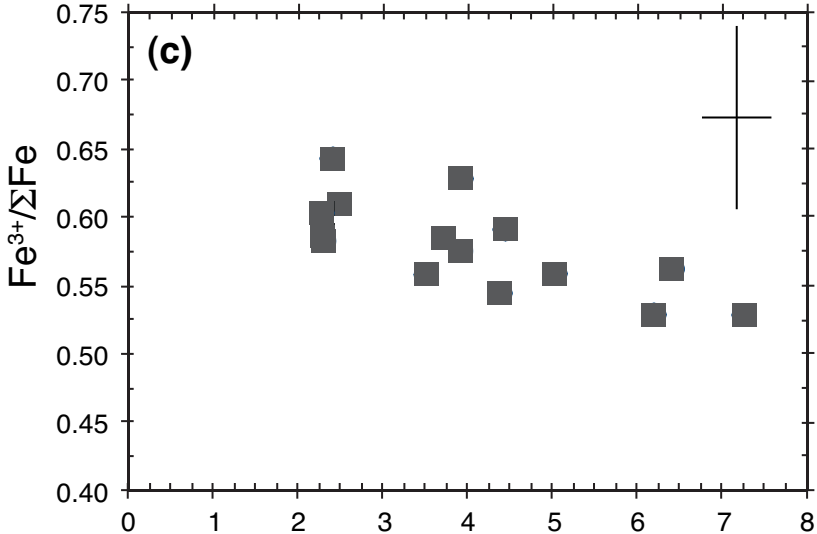
(c)
Fe3+/ΣFe
0.75
0.70
0.65
0.60
0.55
0.50
0.45
0.40
0
1
2
3
4
5
6
7
8

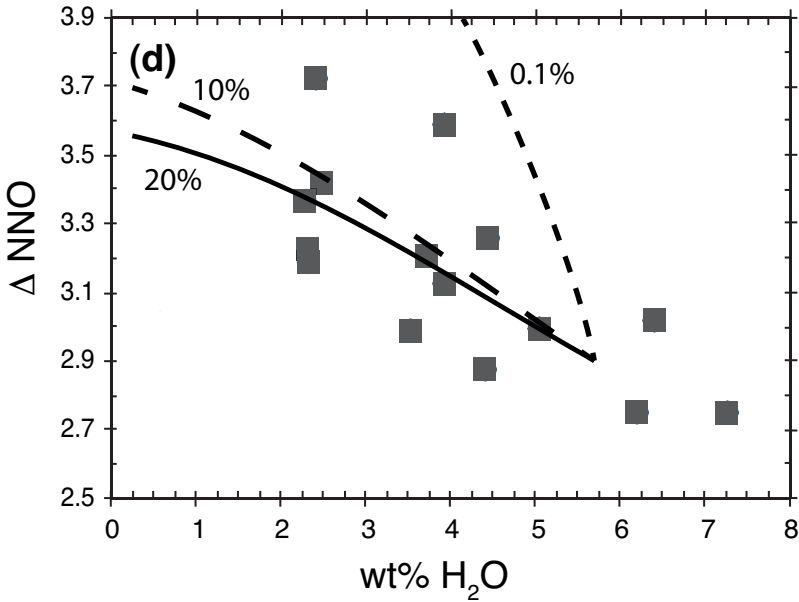
(d)
10%
0.1%
20%
Δ NNO
wt% H2O
3.9
3.7
3.5
3.3
3.1
2.9
2.7
2.5
0
1
2
3
4
5
6
7
8

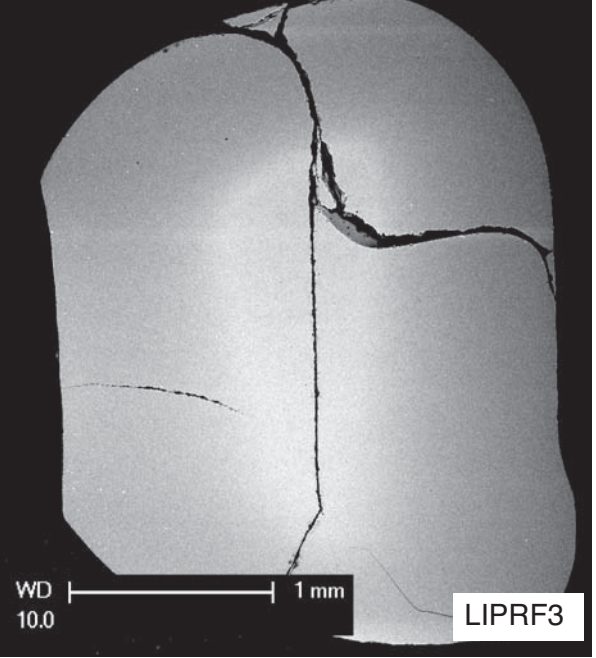
WD
10.0
1 mm
LIPRF3

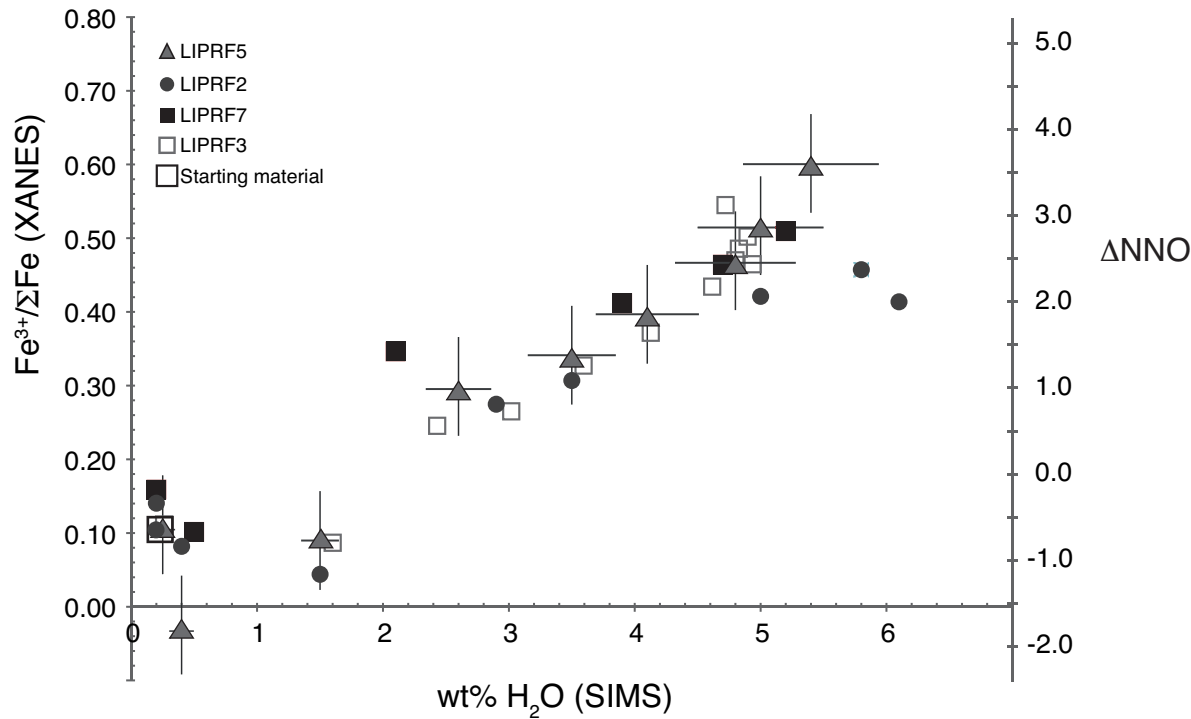
LIPRF5
LIPRF2
LIPRF7
LIPRF3
Starting material
Fe3+/ΣFe (XANES)
0.80
0.70
0.60
0.50
0.40
0.30
0.20
0.10
0.00
0
1
2
3
4
5
6
wt% H2O (SIMS)
5.0
4.0
3.0
2.0
1.0
0.0
-1.0
-2.0
ΔNNO

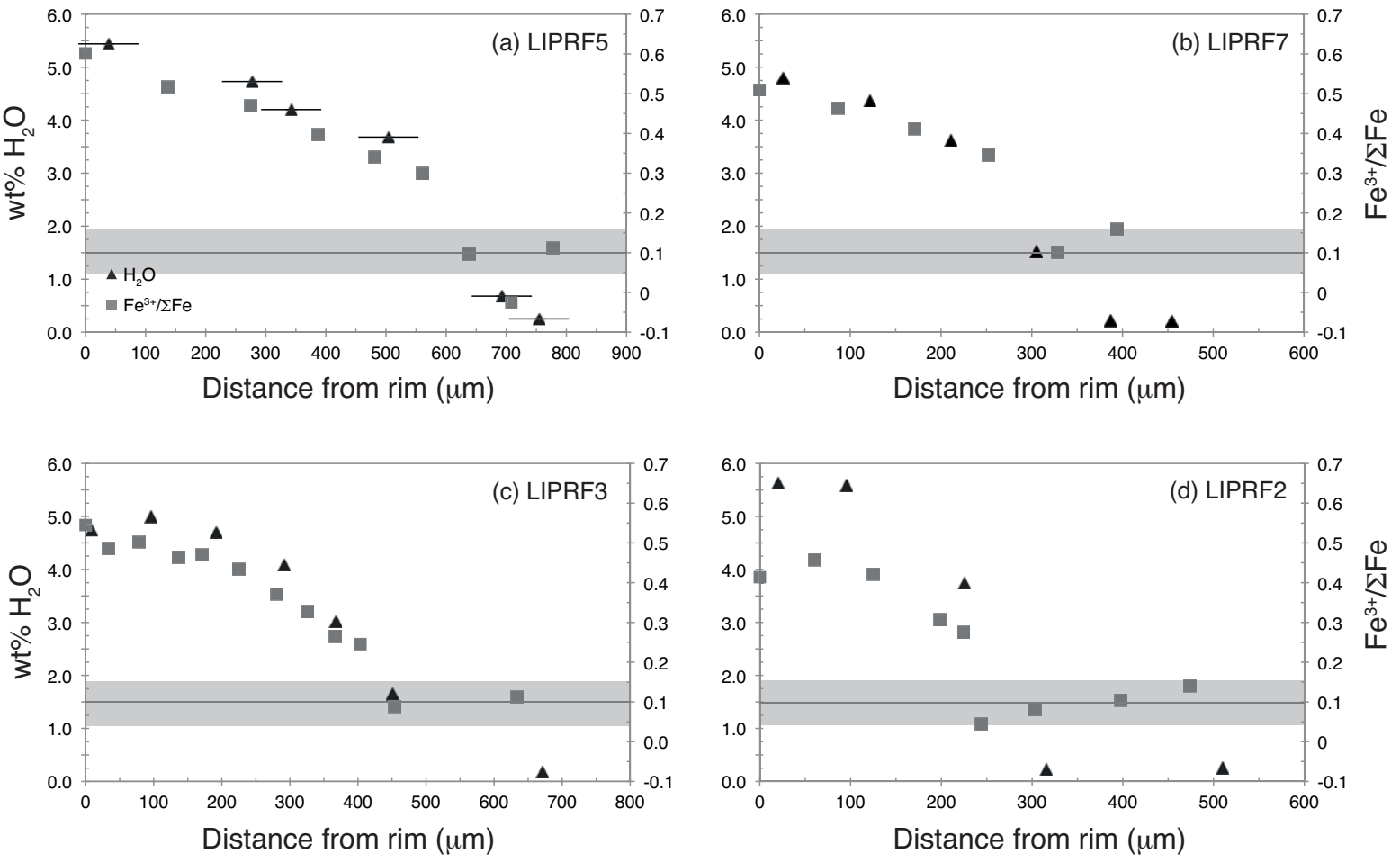
(a) LIPRF5
(b) LIPRF7
(c) LIPRF3
(d) LIPRF2
wt% H2O
Fe3+/ΣFe
H2O
Fe3+/ΣFe
Distance from rim (μm)

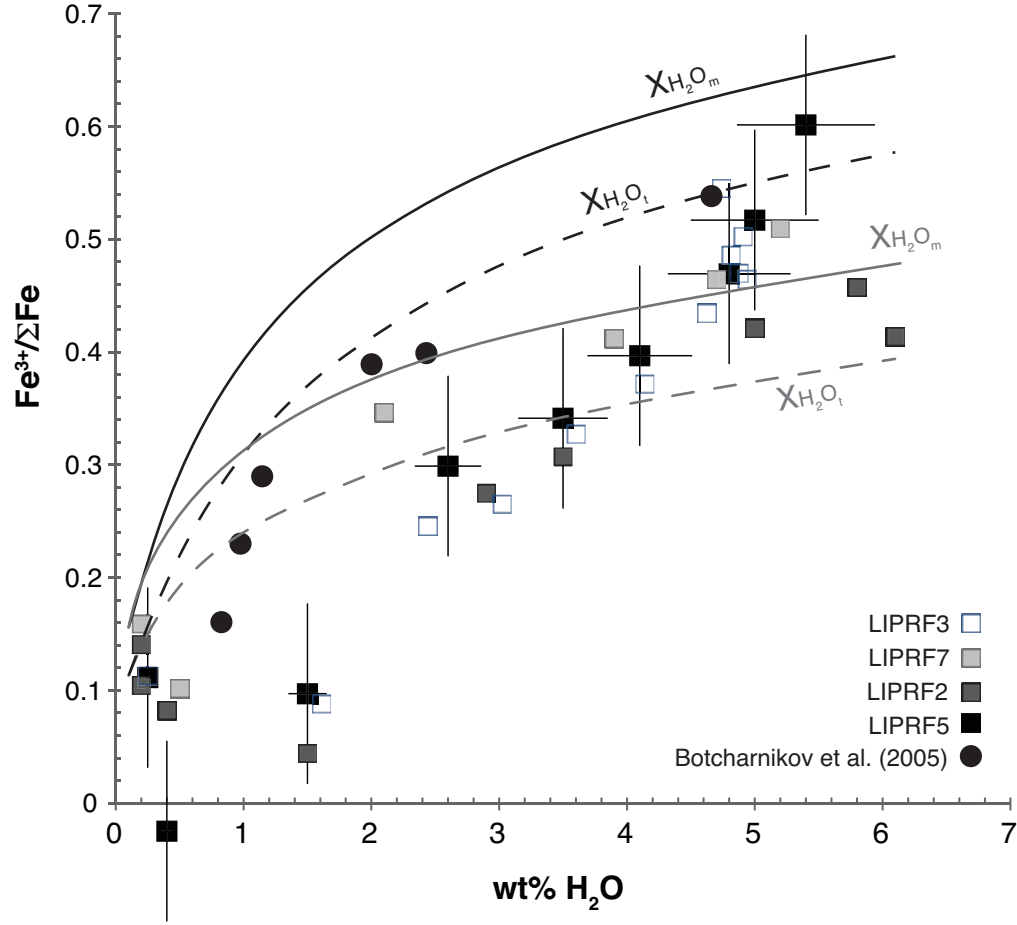
0.7
0.6
0.5
0.4
0.3
0.2
0.1
0
Fe3+/∑Fe
0
1
2
3
4
5
6
7
wt% H2O
XH2Om
XH2Ot
XH2Om
XH2Ot
LIPRF3
LIPRF7
LIPRF2
LIPRF5
Botcharnikov et al. (2005)

Figure 7

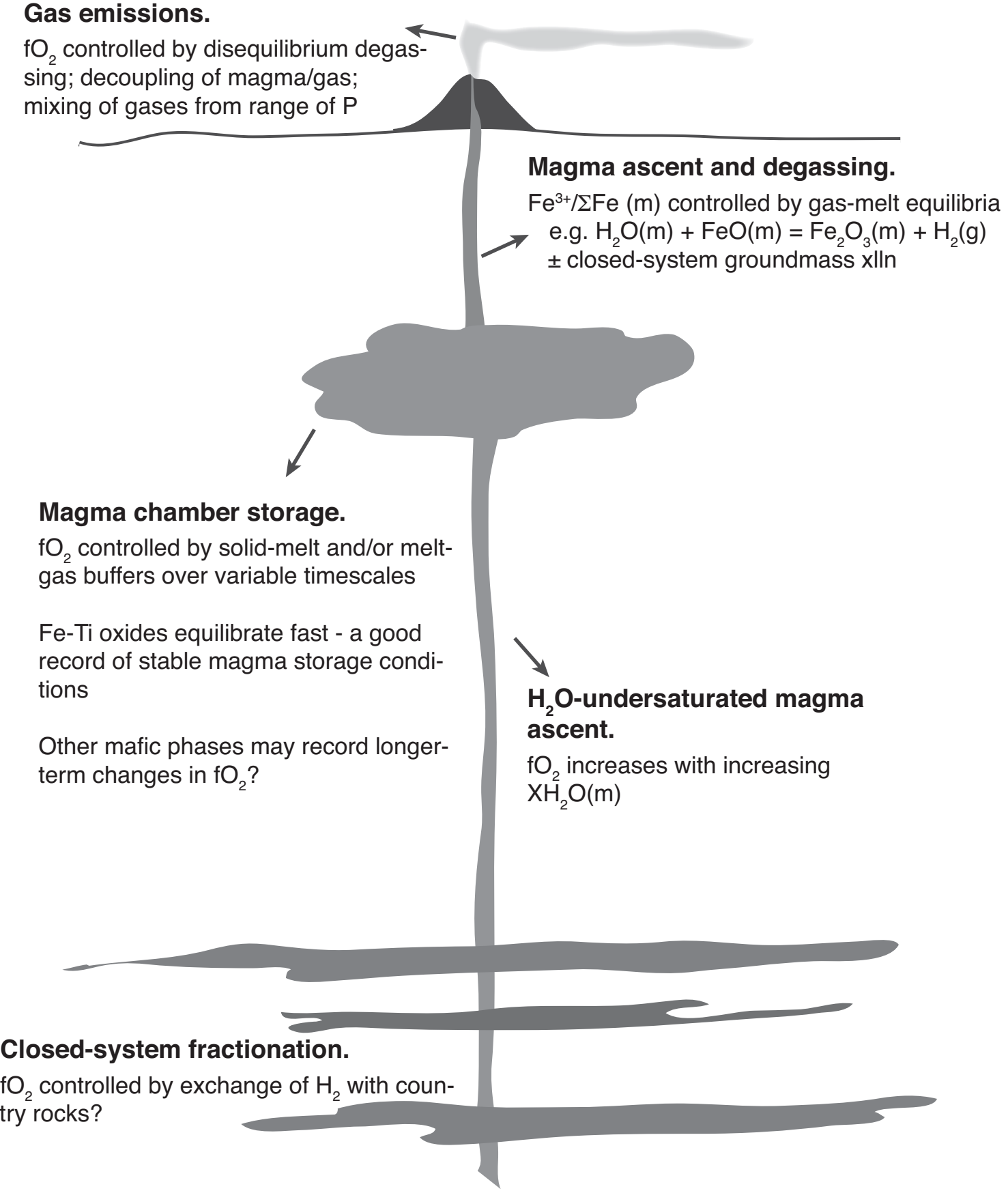
Gas emissions.
fO_2 controlled by disequilibrium degassing; decoupling of magma/gas; mixing of gases from range of P
Magma ascent and degassing.
$Fe^{3+}/\Sigma Fe$ (m) controlled by gas-melt equilibria
e.g. $H_2O(m) + FeO(m) = Fe_2O_3(m) + H_2(g)$
± closed-system groundmass xlln
Magma chamber storage.
fO_2 controlled by solid-melt and/or melt-gas buffers over variable timescales
Fe-Ti oxides equilibrate fast - a good record of stable magma storage conditions
Other mafic phases may record longer-term changes in fO_2?
H_2O-undersaturated magma ascent.
fO_2 increases with increasing $XH_2O(m)$
Closed-system fractionation.
fO_2 controlled by exchange of H_2 with country rocks?

Figure 8

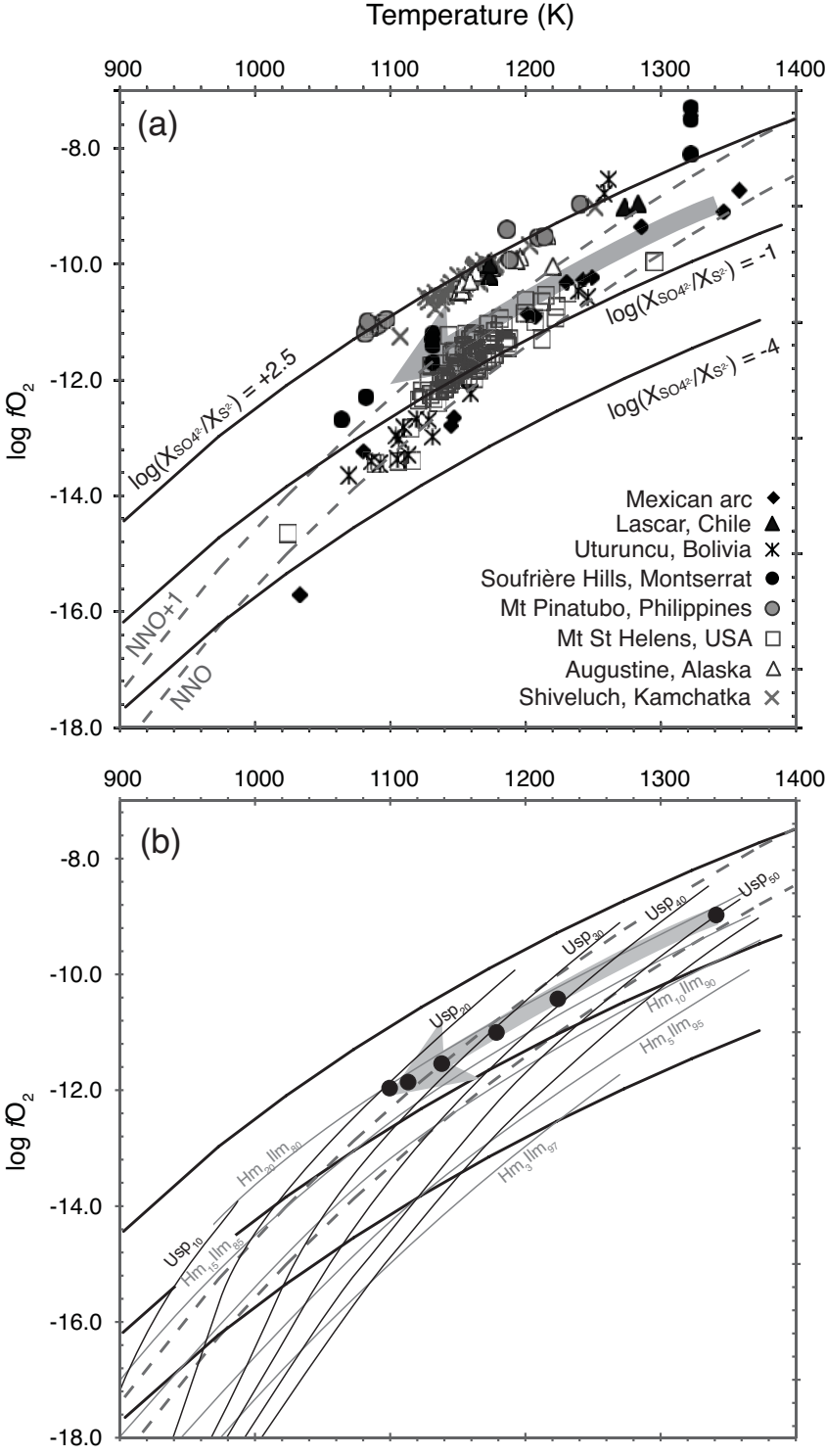
Temperature (K)
900
1000
1100
1200
1300
1400
(a)
-8.0
-10.0
-12.0
-14.0
-16.0
-18.0
log fO2
log(XSO4/XS) = +2.5
log(XSO4/XS) = -1
log(XSO4/XS) = -4
NNO+1
NNO
Mexican arc
Lascar, Chile
Uturuncu, Bolivia
Soufrière Hills, Montserrat
Mt Pinatubo, Philippines
Mt St Helens, USA
Augustine, Alaska
Shiveluch, Kamchatka
(b)
Usp10
Usp20
Usp30
Usp40
Usp50
Hm20Ilm80
Hm15Ilm85
Hm10Ilm90
Hm5Ilm95
Hm3Ilm97

Figure 9

Table 1 - XANES fit components, calculated centroid and total intensity for rhyolite standards. $Fe^{3+}/\Sigma Fe$ values are from Mossbauer spectroscopy (Cottrell et al. 2009).

		Fe^{2+} component						**Fe^{3+} component**								
Analysis number	**Sample**	**Fe^{2+} peak location**	**±**	**Width**	**±**	**Intensity**	**±**	**Fe^{3+} peak location**	**±**	**Width**	**±**	**Intensity**	**±**	**Centroid, eV**	**Total intensity**	**$Fe^{3+}/\Sigma fe$**
8446	DT31	7113.03	0.058	2.098	0.081	0.059	0.004	7114.51	0.012	1.654	0.015	0.136	0.004	7114.12	0.194	0.63
8447	DT18	7113.90	0.038	2.940	0.044	0.141	0.007	7114.52	0.004	1.429	0.013	0.091	0.003	7114.20	0.232	0.66
8448	568_2	7112.81	0.019	1.852	0.033	0.060	0.002	7114.47	0.011	1.622	0.020	0.077	0.002	7113.80	0.137	0.238
8450	DT29	7113.97	0.028	2.741	0.034	0.131	0.004	7114.53	0.005	1.448	0.016	0.097	0.003	7114.27	0.228	0.806
8492	DT39	7112.91	0.024	1.953	0.039	0.073	0.002	7114.50	0.009	1.571	0.016	0.110	0.002	7113.93	0.184	0.315
8494	DT46	7113.03	0.039	2.049	0.059	0.069	0.004	7114.50	0.009	1.554	0.012	0.139	0.003	7114.07	0.207	0.569

Table 2 - (a) Experimental details for Panum dome rhyolite samples from Mangan & Sisson (2000). Pf - final pressure. (b) Experimental details for Lipari obsidian from Humphreys et al. (2008)

Sample	dP/dt, MPa/s	Pf, MPa	Run time (min)	Comments
58	0.025	25	117	Pervasive bubble cloud
63	0.025	100	67	Fringe bubbles only
65	0.025	31	113	Pervasive bubble cloud
68	0.025	175	17	Fringe bubbles only

Sample	P, MPa	T °C	Run time (min)	Comments
LIPRF2	200	857	20	
LIPRF3	200	859	80	
LIPRF5	150	899	67	
LIPRF7	150	901	20	

Table 3 - Electron microprobe compositions of starting glass and experimental run products, reported on anhydrous basis. 1σ uncertainties are derived from electron microprobe analysis. 'n', number of analyses

	Panum dome (Mangan & Sisson 2000)			**Lipari obsidian (Humphreys et al. 2008)**			**Napa Valley Glass Mountain**	
	Starting material	**Avg run products (anhydrous)**	**1 sigma**	**Starting material**	**Avg run products (anhydrous)**	**1 sigma**	**Avg (anhydrous)**	**1 sigma**
SiO_2	75.64	76.94	0.52	74.17	74.39	1.6	76.59	0.51
TiO_2	0.08	0.06	0.02	0.08	0.08	0.03	0.08	0.02
Al_2O_3	12.38	12.56	1.05	12.76	12.95	1.08	12.3	1.03
FeO	0.94	1.01	0.26	1.57	1.59	0.45	1.16	0.27
MnO	0.07	0.05	0.11	0.05	0.07	0.11	0.04	0.1
MgO	0.03	0.03	0.05	0.04	0.04	0.01	0.01	0.05
CaO	0.54	0.54	0.13	0.74	0.75	0.12	0.37	0.11
Na_2O	4.17	3.79	0.53	4.24	4.16	0.73	4.4	0.56
K_2O	4.72	4.94	0.59	5.39	5.49	0.65	4.61	0.56
Cl	0.06	0.07	0.03	0.32	0.31	0.04	0.08	0.03
F				0.16	0.18	0.23		
H_2O	0.17			0.23			0.25	
Total	98.8	99.99		99.75	100.01		99.89	
n		33			110		12	

		Fe^{2+} component						Fe^{3+} component											
Analysis number	**Sample**	**Fe^{2+} peak location**	**±**	**Width**	**±**	**Intensity**	**±**	**Fe^{3+} peak location**	**±**	**Width**	**±**	**Intensity**	**±**	**Centroid, eV**	**Total intensity**	**$Fe^{3+}/\Sigma Fe$**	**wt% H_2O**	**Δ NNO**	**±**
8452	**68-3**	7112.78	0.044	1.886	0.066	0.043	0.003	7114.42	0.013	1.74	0.018	0.124	0.002	7114.05	0.167	0.529	7.27	2.7	0.55
8453	**68-1**	7112.74	0.035	1.840	0.055	0.043	0.002	7114.41	0.010	1.77	0.016	0.129	0.002	7114.05	0.172	0.529	6.20	2.8	0.55
8454	**68-2**	7112.75	0.040	1.808	0.063	0.041	0.003	7114.41	0.011	1.75	0.017	0.134	0.002	7114.08	0.175	0.562	6.42	3.0	0.57
8455	**65-1**	7112.93	0.067	1.983	0.093	0.047	0.004	7114.46	0.014	1.70	0.017	0.145	0.004	7114.15	0.192	0.643	2.41	3.7	0.69
8456	**65-3**	7112.85	0.051	1.915	0.076	0.046	0.003	7114.44	0.012	1.68	0.016	0.137	0.003	7114.10	0.183	0.585	3.72	3.2	0.60
8457	**65-3A**	7112.80	0.050	1.861	0.077	0.043	0.003	7114.42	0.013	1.70	0.018	0.138	0.003	7114.09	0.181	0.575	3.92	3.1	0.59
8458	**65-5A**	7113.00	0.076	2.089	0.103	0.053	0.005	7114.47	0.015	1.67	0.017	0.137	0.004	7114.12	0.190	0.610	2.49	3.4	0.63
8459	**65-7**	7112.81	0.050	1.907	0.075	0.046	0.003	7114.42	0.013	1.70	0.018	0.134	0.003	7114.07	0.180	0.545	4.38	2.9	0.56
8460	**65-9**	7112.92	0.085	1.976	0.119	0.047	0.005	7114.45	0.018	1.69	0.021	0.144	0.005	7114.14	0.191	0.629	3.92	3.6	0.66
8461	**65-8**	7112.87	0.052	1.982	0.077	0.049	0.004	7114.44	0.012	1.68	0.016	0.133	0.003	7114.08	0.181	0.558	3.52	3.0	0.57
8462	**58-3**	7112.96	0.054	2.059	0.076	0.053	0.004	7114.47	0.012	1.67	0.014	0.134	0.003	7114.10	0.187	0.586	2.30	3.2	0.60
8463	**58-2**	7112.94	0.053	2.025	0.074	0.052	0.004	7114.46	0.012	1.68	0.014	0.135	0.003	7114.10	0.186	0.583	2.31	3.2	0.60
8464	**58-1**	7112.93	0.053	1.971	0.076	0.049	0.004	7114.46	0.012	1.68	0.015	0.137	0.003	7114.12	0.186	0.603	2.29	3.4	0.62
8465	**63-1**	7112.83	0.047	1.913	0.070	0.044	0.003	7114.43	0.011	1.71	0.015	0.140	0.003	7114.11	0.185	0.591	4.45	3.3	0.61
8466	**63-3**	7112.74	0.038	1.806	0.060	0.041	0.003	7114.40	0.010	1.74	0.016	0.136	0.002	7114.08	0.177	0.559	5.04	3.0	0.57

Table 4 - XANES fit components, calculated centroid and total intensity, and calculated $Fe^{3+}/\Sigma Fe$ for the high-T decompression samples. H_2O contents are measured from SIMS. Δ NNO is calculated for 900 °C.

		Fe^{2+} component						Fe^{3+} component										
Analysis number	Sample	Fe^{2+} peak location	±	Width	±	Intensity	±	Fe^{3+} peak location	±	Width	±	Intensity	±	Centroid, eV	Total intensity	Distance from rim (μm)	$Fe^{3+}/\Sigma fe$	wt% H_2O (SIMS)
7272	LIRPF5-1	7112.83	0.0285	1.7839	0.0494	0.0416	0.0020	7114.55	0.0078	1.722	0.013	0.139	0.002	7114.11	0.181	0	0.60	5.44
7273	LIPRF5-2	7112.87	0.0303	1.8349	0.0521	0.0479	0.0023	7114.57	0.0099	1.687	0.017	0.120	0.002	7114.04	0.168	136	0.52	5.00
7274	LIRPF5-3	7112.85	0.0259	1.8216	0.0454	0.0498	0.0021	7114.57	0.0094	1.696	0.017	0.113	0.002	7114.01	0.163	274	0.47	4.80
7275	LIPRF5-4	7112.8	0.0207	1.7912	0.0363	0.0510	0.0018	7114.53	0.0083	1.714	0.016	0.111	0.002	7113.95	0.162	387	0.40	4.10
7276	LIPRF5-5	7112.81	0.0209	1.8227	0.0371	0.0551	0.0019	7114.54	0.0091	1.694	0.018	0.104	0.002	7113.90	0.159	482	0.34	3.50
7277	LIRPF5-6	7112.82	0.0187	1.7890	0.0329	0.0572	0.0018	7114.55	0.0093	1.698	0.020	0.096	0.002	7113.86	0.153	561	0.30	2.60
7278	LIPRF5-7	7112.85	0.0170	1.8093	0.0308	0.0673	0.0019	7114.56	0.0119	1.632	0.025	0.073	0.002	7113.70	0.140	638	0.10	1.50
7279	LIPRF5-8	7112.8	0.0144	1.7891	0.0255	0.0701	0.0016	7114.52	0.0115	1.650	0.028	0.067	0.002	7113.60	0.137	708	-0.02	0.40
7280	LIRPF5-9	7112.82	0.0175	1.7884	0.0308	0.0658	0.0019	7114.54	0.0117	1.667	0.027	0.077	0.002	7113.71	0.143	778	0.11	0.25
7281	LIPRF7-1	7112.82	0.0365	1.8057	0.0625	0.0437	0.0026	7114.55	0.0125	1.752	0.022	0.117	0.002	7114.04	0.160	0	0.51	5.20
7282	LIPRF7-2	7112.81	0.0277	1.8060	0.0480	0.0480	0.0022	7114.54	0.0099	1.724	0.018	0.118	0.002	7114.00	0.167	86	0.46	4.70
7283	LIPRF7-3	7112.8	0.0230	1.8522	0.0404	0.0519	0.0019	7114.54	0.0086	1.716	0.015	0.115	0.002	7113.96	0.167	171	0.41	3.90
7284	LIPRF7-4	7112.84	0.0211	1.8498	0.0371	0.0572	0.0019	7114.56	0.0092	1.684	0.017	0.102	0.002	7113.90	0.160	252	0.35	2.10
7285	LIPRF7-5	7112.87	0.0150	1.8345	0.0271	0.0686	0.0017	7114.58	0.0103	1.621	0.022	0.071	0.002	7113.70	0.140	329	0.10	0.50
7286	LIPRF7-6	7112.84	0.0171	1.8011	0.0301	0.0649	0.0018	7114.56	0.0108	1.664	0.024	0.080	0.002	7113.75	0.145	394	0.16	0.20
4660	LIPRF2-1	7112.72	0.0231	1.7718	0.0412	0.0431	0.0017	7114.51	0.0087	1.787	0.018	0.111	0.002	7113.96	0.154	0	0.41	6.10
4662	LIPRF2-2	7112.84	0.0327	1.8514	0.0556	0.0472	0.0025	7114.57	0.0120	1.737	0.021	0.108	0.002	7114.00	0.156	61	0.46	5.80
4663	LIPRF2-3	7112.83	0.0240	1.8290	0.0419	0.0502	0.0020	7114.57	0.0094	1.723	0.018	0.107	0.002	7113.97	0.157	125	0.42	5.00
4664	LIPRF2-4	7112.78	0.0213	1.8283	0.0369	0.0537	0.0018	7114.52	0.0093	1.728	0.019	0.102	0.002	7113.87	0.156	199	0.31	3.50
4670	LIPRF2-5	7112.84	0.0248	1.8271	0.0434	0.0582	0.0023	7114.57	0.0126	1.690	0.026	0.091	0.003	7113.84	0.149	225	0.27	2.90
4665	LIPRF2-6	7112.76	0.0176	1.7885	0.0314	0.0628	0.0018	7114.49	0.0117	1.668	0.026	0.076	0.002	7113.65	0.138	244	0.04	1.50

4666	LIPRF2-7	7112.8	0.0167	1.8094	0.0299	0.0667	0.0018	7114.53	0.0108	1.663	0.025	0.079	0.002	7113.69	0.145	303	0.08	0.40
4667	LIPRF2-8	7112.82	0.0199	1.7933	0.0354	0.0649	0.0021	7114.54	0.0132	1.665	0.029	0.077	0.002	7113.70	0.142	398	0.10	0.20
4668	LIPRF2-9	7112.88	0.0161	1.8471	0.0288	0.0671	0.0017	7114.59	0.0103	1.642	0.022	0.075	0.002	7113.73	0.142	474	0.14	0.20
4671	LIPRF3-1	7112.86	0.0410	1.8802	0.0669	0.0447	0.0028	7114.54	0.0111	1.714	0.017	0.133	0.002	7114.07	0.178	0	0.54	5.40
4672	LIPRF3-2	7112.83	0.0361	1.8774	0.0600	0.0469	0.0026	7114.53	0.0108	1.722	0.018	0.126	0.002	7114.02	0.173	34	0.49	5.40
4673	LIPRF3-3	7112.81	0.0289	1.7642	0.0493	0.0433	0.0021	7114.53	0.0096	1.744	0.018	0.123	0.002	7114.03	0.166	78	0.50	5.30
4674	LIPRF3-4	7112.85	0.0299	1.8570	0.0514	0.0492	0.0023	7114.57	0.0104	1.706	0.018	0.114	0.002	7114.00	0.163	136	0.46	5.00
4675	LIPRF3-5	7112.85	0.0280	1.8431	0.0486	0.0497	0.0023	7114.58	0.0102	1.720	0.018	0.114	0.002	7114.01	0.164	171	0.47	4.80
4676	LIPRF3-6	7112.83	0.0277	1.8342	0.0491	0.0505	0.0023	7114.57	0.0105	1.711	0.019	0.111	0.002	7113.98	0.162	225	0.43	4.70
4677	LIPRF3-7	7112.83	0.0288	1.8502	0.0504	0.0521	0.0024	7114.54	0.0112	1.685	0.020	0.105	0.002	7113.92	0.158	281	0.37	4.70
4678	LIPRF3-8	7112.74	0.0263	1.7600	0.0472	0.0507	0.0023	7114.5	0.0112	1.729	0.024	0.108	0.002	7113.89	0.159	326	0.33	4.40
4679	LIPRF3-9	7112.78	0.0196	1.7886	0.0349	0.0548	0.0018	7114.51	0.0094	1.700	0.019	0.097	0.002	7113.84	0.152	367	0.27	4.40
4680	LIPRF3-10	7112.81	0.0239	1.8159	0.0407	0.0575	0.0022	7114.53	0.0123	1.709	0.025	0.092	0.002	7113.82	0.150	404	0.25	4.00
4681	LIPRF3-11	7112.81	0.0156	1.7353	0.0271	0.0617	0.0016	7114.53	0.0114	1.698	0.027	0.073	0.002	7113.69	0.135	454	0.09	3.60
4682	LIPRF3-12	7112.83	0.0161	1.7828	0.0293	0.0647	0.0017	7114.56	0.0108	1.647	0.024	0.075	0.002	7113.71	0.140	633	0.11	0.90
7287	Starting material	7112.81	0.0155	1.7998	0.0274	0.0657	0.0017	7114.54	0.0103	1.669	0.023	0.077	0.002	7113.70	0.143		0.10	0.23

Table 5 - XANES fit components, calculated centroid and total intensity, and calculated $Fe^{3+}/\Sigma Fe$ for the high-T hydration samples. H_2O contents are measured from SIMS.

Analysis number	XANES analysis	SIMS analysis	Distance (microns)	±	Fe^{2+} component						Fe^{3+} component						Centroid, eV	Total intensity	$Fe^{3+}/\Sigma Fe$	H_2O wt% (SIMS)	H_2O wt% (greyscale)
					Fe^{2+} peak location	±	Width	±	Intensity	±	Fe^{3+} peak location	±	Width	±	Intensity	±					
4650		NVGM_1	-515	**50**	7112.87	0.022	1.853	0.038	0.061	0.002	7114.59	0.010	1.683	0.021	0.100	0.002	7113.89	0.160	0.33	0.27	
8486		NVGM_2	-279	50	7112.85	0.027	1.945	0.044	0.062	0.002	7114.48	0.010	1.631	0.019	0.099	0.002	7113.91	0.161	0.36	0.28	
		NVGM_3	-64	10	7112.79	0.027	1.850	0.043	0.053	0.002	7114.45	0.010	1.694	0.019	0.110	0.002	7113.97	0.163		0.29	
8482	NVGM_3		-112	25	7112.79	0.027	1.850	0.043	0.053	0.002	7114.45	0.010	1.694	0.019	0.110	0.002	7113.97	0.163	0.43		0.68
		NVGM_4	-35	10																0.96	
8483	NVGM_4		-80	25	7112.83	0.026	1.927	0.042	0.055	0.002	7114.47	0.009	1.665	0.014	0.109	0.002	7113.98	0.164	0.44		0.48
		NVGM_5	55	10																2.79	
		NVGM_6	22	10																3.05	
8484	NVGM_6		10	10	7112.8	0.032	1.873	0.052	0.050	0.002	7114.46	0.010	1.673	0.017	0.116	0.002	7114.02	0.165	0.49		1.9
8485	NVGM_7	NVGM_7	148	25	7112.83	0.029	1.939	0.044	0.048	0.002	7114.46	0.009	1.697	0.013	0.111	0.002	7114.03	0.160	0.50	3.33	
8487	NVGM_4A		-58	10	7112.8	0.035	1.887	0.053	0.049	0.003	7114.45	0.012	1.722	0.020	0.113	0.003	7114.01	0.163	0.47		0.64
4651			-300	50	7112.87	0.017	1.880	0.030	0.060	0.002	7114.54	0.008	1.633	0.013	0.095	0.001	7113.84	0.155	0.27		0.27
4686			-300	50	7112.88	0.025	1.899	0.044	0.061	0.002	7114.56	0.010	1.643	0.018	0.104	0.002	7113.89	0.164	0.33		0.27
4687	NVGM_9		30	50	7112.8	0.034	1.823	0.056	0.041	0.002	7114.52	0.011	1.784	0.019	0.117	0.002	7114.03	0.158	0.49	2.25	
4688	NVGM_8		30	50	7112.87	0.045	1.895	0.073	0.044	0.003	7114.57	0.014	1.748	0.021	0.120	0.003	7114.06	0.164	0.54	2.53	

Table 6 - XANES fit components, calculated centroid and total intensity, and calculated $Fe^{3+}/\Sigma Fe$ for the low-T hydration samples.
H2O contents are measured from SIMS or estimated from greyscale calibrations. Distance is measured relative to a prominent crack in the sample rim (see figure 7).